

Second Edition

**Handbook of
FLUID
DYNAMICS**

**Edited by
RICHARD W. JOHNSON**



CRC Press

Taylor & Francis Group
Boca Raton London New York

CRC Press is an imprint of the
Taylor & Francis Group, an **informa** business

Particle Image Velocimetry

48.1	Introduction	48-1
48.2	Strengths and Weaknesses of PIV.....	48-2
	Strengths • Weaknesses	
48.3	Fundamentals of PIV Algorithms.....	48-3
	Image Pairs • Spatial Cross-Correlation • Subpixel Interpolation • Interrogation Region Overlap, Multipass, and Multigrid • Vector Postprocessing	
48.4	Designing a PIV Experiment.....	48-7
	Modes of PIV Image Acquisition • Camera Basic: Characteristics of Digital Camera Sensors • Camera Types • Lasers • Timing • Tracer Particles for PIV Seeding • Optics	
48.5	Best Practices for Good Measurements	48-20
	Choosing the Time between Images dt • Choosing Interrogation Region Size • Adjusting Particle Image Diameter • Seed Image Density • Determining Origin • Illumination Issues • Image Preprocessing	
48.6	Stereo Particle Image Velocimetry.....	48-22
	SPIV Optics • SPIV Calibration • Pinhole Calibration Model • Polynomial Calibration Model • Stereo Self-Calibration • SPIV Reconstruction	
	References.....	48-25

Barton L. Smith
Utah State University

Douglas R. Neal
LaVision Inc.

48.1 Introduction

Early fluid dynamicists used flow visualization techniques to gain a qualitative understanding of the complex phenomena they were studying. Until nearly the end of the twentieth century, quantitative flow measurements were only possible through the use of point measurement techniques such as vane anemometers, pressure (Pitot) probes, hot-wire anemometry (HWA), and laser Doppler velocimetry (LDV). In the early 1980s, the advent of particle image velocimetry (PIV) created a new technique for gathering quantitative data from fluid flow images. PIV allowed for whole-field, instantaneous measurements of velocity, which added quantitative information to visual representations of fluid flow. Throughout the 1990s and into the early twenty-first century, advances in digital image processing made it possible to extract useful data from nearly every kind of flow image, adding a new level of accuracy to rival point measurements (Neal et al., 2014). PIV subsequently emerged as one of the most powerful flow diagnostic tools for fluid dynamics research. Today, its popularity has extended well beyond traditional fluid dynamics research labs, branching out into disciplines as diverse as zoology, oceanography, geophysics, and marine biology (Blois et al., 2014; Drucker and Lauder, 1999; Frank et al., 2008; McNutt et al., 2012).

While there are many ways to implement a PIV system, the most common two-component (2C) PIV system is shown in

Figure 48.1. A laser beam is converted into a light sheet through a cylindrical lens. The sheet illuminates particles in a flow that are in turn imaged by a digital camera. Throughout this chapter, we will refer to the coordinate system described in this figure wherein the laser illuminates the xy -plane.

As stated by Klewicki (2007: 902), “PIV is a technique synonymous with compromises.” While performing PIV measurements, one must be keenly aware of which parameters are flexible and which must be optimized, since improving any aspect of the measurement often impacts another negatively. PIV practitioners of all levels of experience will find that an increased understanding of the details of PIV will yield considerably better data; however, this chapter is designed to be a concise guide for the beginner. It is anticipated that more detail may be desired on every topic. It is the authors’ experience that such a level of detail can impose a significant barrier to a working knowledge of the technique. There are numerous advanced texts that can provide more rigorous detail for the experienced user. These texts are referenced throughout this chapter.

This chapter is intended as a primer to new users and potential new users of PIV. In it, the reader will find an explanation of how PIV works starting at the most fundamental level and moving on to sophisticated, modern algorithms. Next, information to aid someone seeking a velocity measurement system, including the pros and cons of PIV and information about a system’s components, will be provided. Finally, more advanced PIV

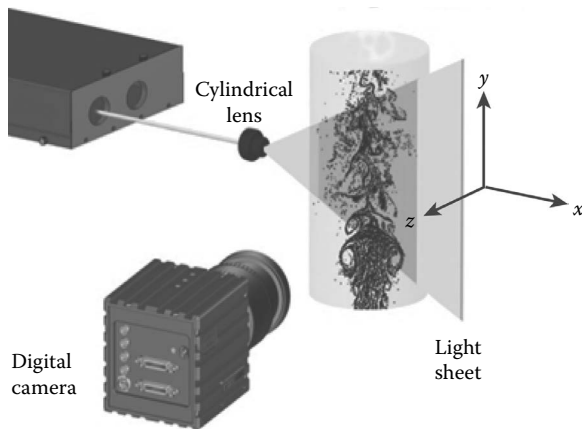


FIGURE 48.1 Schematic of a typical 2C PIV system consisting of a laser, cylindrical lens, and a digital camera. The laser fires in the x direction and is spread into a sheet in the y direction. This coordinate system will be used throughout the chapter.

techniques, such as stereo particle image velocimetry (SPIV), will be briefly discussed. The chapter focuses on modern equipment and algorithms and will not revisit methods/hardware that have become obsolete due to new technology (e.g., a photographic film). A comprehensive history of PIV will not be revisited here as several excellent PIV histories already exist (Adrian, 1991, 2005; Raffel et al., 2007).

48.2 Strengths and Weaknesses of PIV

The strengths and weakness of PIV relative to several popular velocity measurement techniques will now be described. These other methods include HWA and LDV.

48.2.1 Strengths

The most often-cited advantage of PIV is the unobtrusive nature of the measurement, which is a feature it shares with LDV. While one does need to introduce seed particles to the flow, they have a low number density and rarely impact the flow. In some rare instances involving very slow flow, heating by the laser sheet may influence the velocity field and sometimes, it can be difficult to introduce a seed without adding momentum to the flow, but in the vast majority of circumstances, PIV measurements have essentially no impact on the flow.

PIV is a radical departure from traditional velocity measurement techniques in that it provides a velocity *field* at an instant in time as opposed to the time-varying velocity at a point in space that is provided by HWA and LDV. This allows the user to see flow structure, which is lost in time-varying point measurements. Similar to time-varying point measurements, the vector fields may be averaged to determine the time-averaged flow field. Since PIV measurements have a high frequency response, the individual fields may also be used to determine velocity statistics such as Reynolds stresses, even when the data are acquired at rates far below the important temporal frequencies in the

flow. This point may appear counterintuitive if data rate is confused with frequency response. In fact, when collecting data for computing statistics, slow sampling better ensures statistically independent samples and faster convergence of the statistics (Tennekes and Lumley, 1972).

A third strength of PIV is the broad range of flows to which it can be applied. PIV can be performed well in liquids or gases and at scales from micrometers to tens of meters. PIV measurements can be made in any transparent medium with optical access. The spatial resolution of PIV is not fixed and may be altered through optics. This flexibility is why PIV is the only velocity-measuring system used in many fluid dynamics laboratories.

At the small scale, PIV is limited by the size of the tracer particles (cf. Section 48.5.3). At the large scale, PIV is also limited by the tracer size, which must be large enough to scatter sufficient light while remaining neutrally buoyant. For example, in very large fields of view (FOV), helium-filled soap bubbles (HFSBs) are often used as tracer particles (Bosbach et al., 2009).

48.2.2 Weaknesses

48.2.2.1 Dynamic Range

Compared to any other measurement technique, the dynamic velocity range (DVR), or the maximum measurable velocity divided by the velocity accuracy of PIV, is very poor; typically 160:1 for modern algorithms. One has little control over the accuracy while the maximum measurable velocity is fixed by the choice of dt and the 160:1 estimate assumes an optimal choice. Failure to maximize dt makes the poor DVR of PIV worse.

To achieve an acceptable DVR, one must take care to use the full range through optimization of dt as described in Section 48.5.1. In many cases (e.g., wakes and jets), the flow itself covers a large dynamic range and it may not be possible to optimize the dt over the entire measurement region. For a sufficient frame rate, multiple pairs of images may be used to improve the dynamic range by pairing the first and third or fourth frame in regions of slow flow that require a larger dt (Persoons and O'Donovan, 2011; Scarano and Moore, 2012; Sciacchitano et al., 2012) to achieve acceptable particle displacements. Using this method, the dt is not fixed for the entire measurement region.

48.2.2.2 Uncertainty Quantification

PIV measurements can be accomplished within hours by a novice using turnkey commercial systems. Most PIV software can produce a vector field that may appear reasonable from very poor raw data. It is a common practice that only the final vector field, after many passes and postprocessing that may include vector replacement and smoothing, is examined before the data are deemed acceptable. Conversely, while turnkey HWA and LDV systems are also commonly available, these systems consist of parts and software that can require significant expertise before one can acquire data (i.e., tuning a hot wire or aligning an LDV probe can be a very difficult task).

This relative ease of use has created the opinion (in some communities) that PIV is less accurate than other techniques. While the PIV community has spent considerable time on the *a priori* accuracy of PIV as a function of a few parameters, until recently, no effort had been made to determine the *a posteriori* uncertainty of a PIV measurement. Four methods for determining *a posteriori* uncertainty have now appeared (Timmins et al., 2012; Charonko and Vlachos, 2013; Sciacchitano et al., 2013; Wieneke, 2014) making it practical to quantify the accuracy of a measurement and to demonstrate that PIV measurements performed by well-trained personnel have uncertainty that is very competitive with other experimental techniques. These four methods have been evaluated as part of an international collaboration on PIV uncertainty. The results of this collaborative effort are described in Neal et al. (2014) and Sciacchitano et al. (2015).

48.2.2.3 Optical Access Requirements

PIV requires a transparent medium in which a laser sheet can be formed that can in turn be imaged with no more distortion than can be corrected in a calibration procedure. As a result, PIV has not been achieved in many important flows, including liquid metals, high-void fraction bubbly flows, or near-field sprays.

48.2.2.4 Seeding Requirements

While seeding is a trivial issue for many PIV experiments, it can also be a major issue in others. For gases, seed particles may have too much inertia compared to their drag to accurately track the flow, or they might evaporate due to high temperatures, or they can be flammable. Especially in gases, seed particles may be too small to reflect sufficient light. Any flow may involve insufficient mixing to disperse the seed uniformly, and seeds may be carcinogenic or may build up on surfaces over time. Some of these issues present expense and difficulty in an experimental setup, while others may impact the accuracy of the computed vector field.

While its unobtrusive nature is an often-cited strength of PIV, one must be careful to not alter the flow of interest in an

effort to seed it sufficiently and uniformly. Especially in low Reynolds number flows, this can be quite challenging. Section 48.4.6 below provides information on seeding methods that may be helpful.

48.3 Fundamentals of PIV Algorithms

This section will describe PIV processing at its most basic level. A PIV measurement consists of a pair of particle images contained inside an interrogation region (a small portion of a digital picture) acquired at a short time interval dt apart. PIV seeks to determine the most probable displacement $d\vec{x}$ of the fluid inside the interrogation region during the known time interval dt over which the two images were acquired by assuming that the particles follow the flow. A spatial cross-correlation operation is used to estimate the displacement $d\vec{x}$ of the particles within the interrogation region during the interval dt .

48.3.1 Image Pairs

While a PIV data campaign may involve hundreds or thousands of images, each measurement is formed from a pair of images, one acquired prior to the other. For a typical image pair, some time is allowed to elapse between the acquisition of the two images. This elapsed time between images is known as the dt between the image pairs. With some PIV systems, it may be advantageous to form a pair with the first and second image, a second pair with the second and third image, and so on. These different timing schemes are described in Section 48.4.1. The time interval between the images is generally controlled through laser timing and has a very substantial impact on the quality of the measurement, as described in Section 48.5.

Although other image acquisition methods were used in the early years of PIV, modern PIV measurements nearly always use grayscale digital images that are acquired by digital cameras. A digital image pair is illustrated for the simple case of single-pixel, binary particle images that are less than one pixel in diameter (Figure 48.2). By “binary,” we mean that the pixel has either a

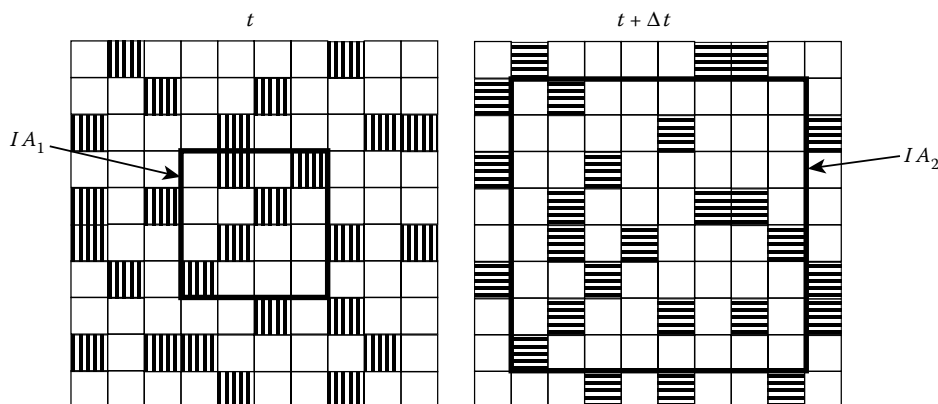


FIGURE 48.2 Interrogation region acquired at two different points in time. Each square represents one pixel on the camera sensor. The dark lines indicate the boundaries of the interrogation regions discussed in the description of Figure 48.4. The flow is two pixels down and two to the left.

value of 0 or 1, or is “on” or “off.” Real digital cameras have many gray levels that are specified by the number of bits. The number of gray levels for a camera sensor are 2^{bits} as discussed below in [Section 48.4.2](#). A binary camera has a single bit and therefore 2^1 possible levels.

Binary bit depth and single pixel particle image size would be nonideal and are presented only for simplicity. While it may not be immediately apparent, one can confirm that the flow is down and to the left. Determining this displacement is the most fundamental task of a PIV algorithm and is typically performed using a spatial cross-correlation as described below.

For this simple case, no particles have left the laser sheet (by traveling in the z direction) during dt . All of them appear at both instances, except near the image edges, where particles may move into or out of the interrogation region between the two time instances. In real flows, through-plane motion of the time-averaged or fluctuating velocity will cause some particle images to appear in one image and not the other. Mismatch of the location of the laser sheet of the two lasers can cause a similar effect, as discussed in [Section 48.5.6](#).

In real measurements, particle images are grayscale with many possible values of intensity (e.g., 256 for an 8-bit camera and 4096 for a 12-bit camera). Generally, it is preferable that particles images are larger than one pixel and for a large seeding density they commonly overlap. An example of one time instance of actual PIV data is shown in [Figure 48.3](#).

The image spatial units are pixels, but these may be easily converted into meters through a calibration. For single-camera PIV with the camera normal to the laser sheet and a sufficiently narrow viewing angle, calibration can be performed simply by acquiring an image of an object of known size, such as a ruler.

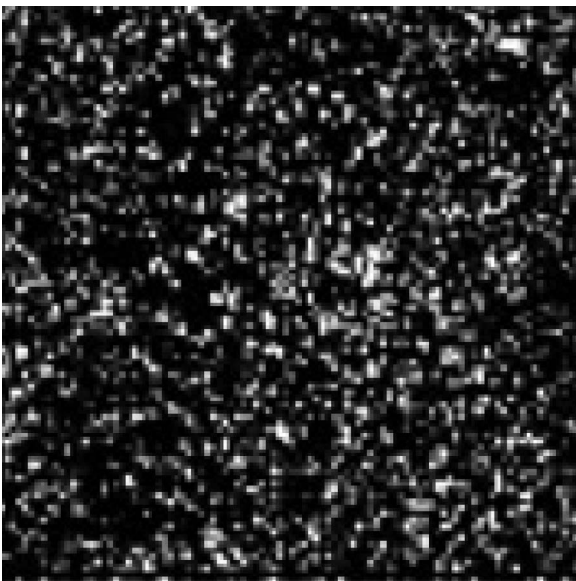


FIGURE 48.3 A small portion of an actual PIV image.

48.3.2 Spatial Cross-Correlation

Effective use of PIV is not possible without a fundamental understanding of the cross-correlation operation on which it is based. The spatial cross-correlation returns the most probable value of displacements of objects in the interrogation region (Westerweel, 1997; Raffel et al., 2007)

$$R(r, s) = \sum_{i=0}^{D_I/2} \sum_{j=0}^{D_I/2} I_{A_1}(i, j) I_{A_2}(i + r, j + s) \quad (48.1)$$

where D_I is the size (in pixels) of the first square interrogation region, I_{A_1} and I_{A_2} are the intensity values from the first and second image, respectively, and we choose, somewhat arbitrarily, that $r, s = -D_I/2 \dots D_I/2$. Given this choice, the size of the correlation plane R is $(D_I + 1) \times (D_I + 1)$. While the correlation map could be computed for a larger area, the likelihood of finding a valid correlation at larger values of r and s diminishes as r and s grow beyond $D_I/2$.

Equation 48.1 says that for each value of r and s , the magnitude of the cross-correlation is the double sum of the product of the two images, with the second image shifted in space by r and s . It is helpful to visualize the two image fields overlaid at various r and s “shifts.” This is illustrated using the same hypothetical image pair discussed above and shown in [Figure 48.4](#). Again, note that these images are binary, meaning a hatched pixel has a value of 1 while white indicates 0. The interrogation region size of I_{A_1} is $D_I = 4$ pixels high and wide. The location of the interrogation region is indicated by the heavy-lined square in [Figure 48.4](#). The hatch patterns from the two images are in different directions so that they may be differentiated. For $r = s = -2$, one illuminated pixel overlaps in both images (indicated by cross-hatching), and therefore, the correlation value for these r and s values is 1. A similar illustration can be made for each combination of r and s . For $r = s = 0$, two particle images overlap. For $r = -2$, $s = 2$, five particle images overlap. Since this is the largest correlation value found, this is interpreted as the most likely displacement during dt to pixel accuracy. Subpixel accuracy can be achieved using the methods described below.

The situation described in [Figure 48.4](#) is highly simplified. Cameras commonly have bit depth above 8 and, ideally, particle images straddle several pixels and much larger interrogation regions are normally used to ensure sufficient correlated particle images. However, the points made in the discussion above are as valid for these more complex situations.

Equation 48.1 is a *direct* cross-correlation, which is expensive for large interrogation regions when computed using central processing unit (CPU) hardware. For this reason, the convolution theorem (James, 2011) is commonly employed to allow the correlation to be computed using superefficient fast-Fourier transforms (FFTs). The correlation theorem states that multiplying the Fourier transform of one function by the complex conjugate of the Fourier transform of the other gives the Fourier transform

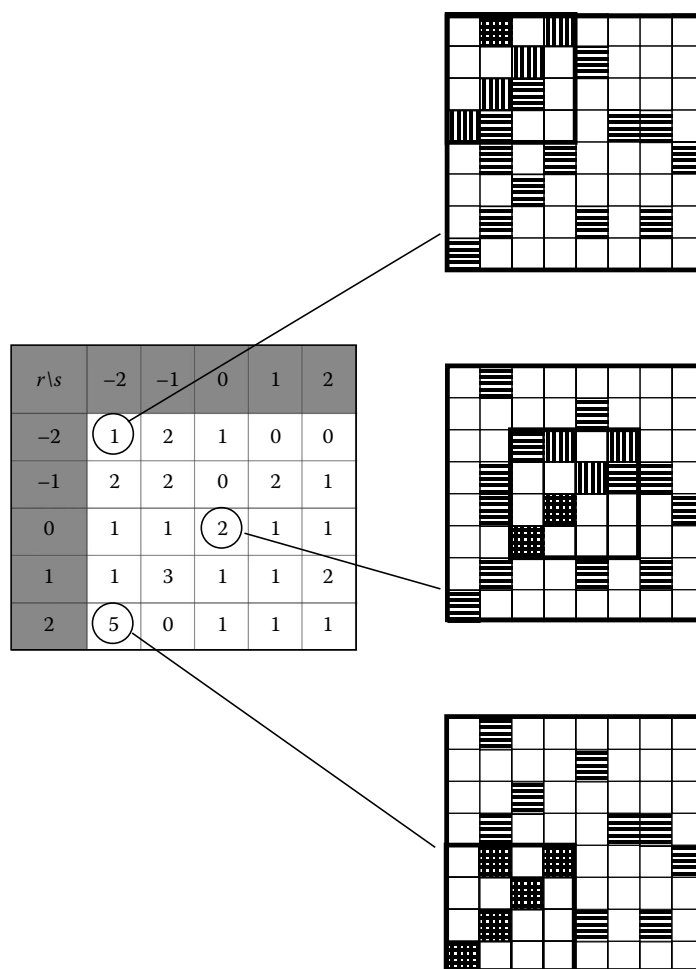


FIGURE 48.4 Illustration of the cross-correlation map R (left) using the two images in Figure 48.2 for $r = s = -2$, $r = s = 0$, and $r = 2, s = -2$. For the simple case of a binary sensor and single-pixel particle images, the correlation value is simply the total number of particle images that overlap when IA_2 is shifted by r and s as indicated in the correlation map of R at the left.

of their cross-correlation. That is, we take both signals into the frequency domain, form the complex conjugate of one of the signals, multiply, and then take the inverse Fourier transform. By the convolution theorem, $R \Leftrightarrow IA_1 \cdot IA_2^*$, where the carrot indicates the Fourier transform, $*$ indicates the complex conjugate, and the double arrow indicates a Fourier transfer pair. As a result, D_f is often chosen to be a power of 2, as required by FFTs. In some cases, a region of a size that is a power of two is generated by padding the exterior of the interrogation region with zeros.

48.3.3 Subpixel Interpolation

Dynamic range is the maximum measurable value divided by the lowest measurable value. Since PIV measurements are usually based on particle displacements of 10 pixels or fewer, PIV has a limited dynamic range, as described in Section 48.2.2, with much of the dynamic range relying on the ability to determine the displacement with subpixel accuracy. Our ability to do so stems from knowledge of the expected shape of the

cross-correlation peak. For diffraction-limited particles (cf. Section 48.5.3), the particle images are nearly Gaussian (Raffel et al., 2007) and the cross-correlation of Gaussian images is also Gaussian (Adrian and Westerweel, 2011). By fitting the peak in the cross-correlation R to a Gaussian function, we may determine the subpixel location of its peak as shown in Figure 48.5. We note that this figure depicts an actual cross-correlation peak and has no connection to the simplified Figure 48.4.

Subpixel estimation is performed for each direction independently and for the following discussion, we will limit attention to the r direction. We again note that no meaning is ascribed to the magnitude of R , but rather, the r, s location of the maximum value of R is interpreted as the most likely displacement for the particles in that interrogation region, with the displacement measured in pixels. Pixel units may be converted into spatial units through the calibration.

Curve fitting for each component of each vector is expensive, but fortunately not necessary. Assuming a Gaussian distribution of the correlation R with standard deviation σ

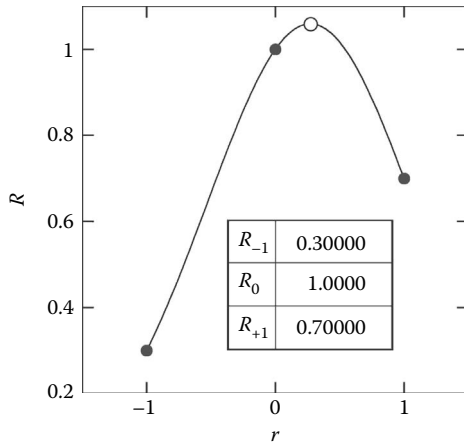


FIGURE 48.5 Curve fit of a Gaussian function (Equation 48.2) to the correlation peak and its neighbors (filled dots). The fit indicates that the center of the Gaussian (open dot) is 0.27 pixels to the right of the peak. The magnitude of the three points is shown in the inset table. These may be used in the algebraic equation Equation 48.3 to determine the subpixel displacement without curve fitting.

$$R = 1/(\sigma\sqrt{2\pi})\exp(-\frac{1}{2}((x-\mu)/\sigma)^2) \quad (48.2)$$

One can linearize the Gaussian function by taking the log of both sides of the equation

$$\ln R = \ln\left(\frac{1}{(\sigma\sqrt{2\pi})}\right) - \frac{1}{2}((x-\mu)/\sigma)^2$$

and substituting

$$A = -1/(2\sigma^2)$$

$$B = +2\mu/(2\sigma^2)$$

$$C = \ln(1/(\sigma\sqrt{2\pi})) - \frac{1}{2}(\mu/\sigma)^2$$

so that our equation becomes

$$Ar^2 + Br + C$$

For the simple case of three equally spaced points, the (r, R) data can be used to solve a set of three equations to obtain

$$\varepsilon = \frac{\ln R_{-1} - \ln R_{+1}}{2(\ln R_{-1} - 2\ln R_0 + \ln R_{+1})} \quad (48.3)$$

where ε is the subpixel displacement in the r direction, R_{-1} and R_{+1} are the correlation values at the points neighboring the peak in the r direction and R_0 is the peak value. This operation

is performed for each vector in the r and s directions independently (Raffel et al., 2007; Westerweel, 1993). The accuracy of this method is somewhat debatable and certainly depends on the algorithm employed as well as flow and image conditions, but is normally between 0.1 and 0.01 pixels.

48.3.4 Interrogation Region Overlap, Multipass, and Multigrid

A vector is computed at each grid location using the scheme outlined above. The grid of vector locations is computed for each velocity field as a function of the interrogation region size D_i as well as the “overlap.” Counter to other measurement techniques, it is common to “oversample” the velocity field by using overlapping interrogation regions. This is justified since the displacement calculation is a much stronger function of the center of the interrogation region than its edges. Overlapping interrogation regions by 50%–75% is common. The resultant spatial resolution is discussed in Scarano (2003) and depends on the spatial curvature of the velocity distribution. If the information in each overlapped interrogation region that is used in the correlation is indeed independent, then, overlap improves spatial resolution.

Furthermore, since the late 1990s, it has been common to use multipass schemes that take the vector computation from the first pass to either displace the second interrogation region (Westerweel et al., 1997) or to deform it (Scarano, 2002) on subsequent passes. This eliminates the need to adhere to the quarter rule (requiring that all displacements are 1/4th the interrogation region size) for the final pass and permits a reduction in the final interrogation region size (multigrid), thus improving spatial resolution and decoupling the dynamic range from spatial resolution.

48.3.5 Vector Postprocessing

Vector postprocessing consists of removal of “bad vectors” and replacement of the missing data. Even when PIV data are acquired using the best practices, occasionally, something other than the particle field displacement results in the largest peak in the correlation. In such a situation, the resultant vector can face in an arbitrary direction and have a magnitude very different than the real flow. Spurious correlation occurs when the signal from the particle images is weaker than other correlation sources, such as the background or even image sensor noise. This may be due to large background effects (such as laser sheet flare) or due to an insufficient particle number or illumination. It is always necessary to remove “bad vectors.” Failure to do so can cause large errors in time-averaged quantities, especially for Reynolds stresses. Since such bad vectors generated by spurious correlation are usually quite different than their neighbors, they can be identified and eliminated using several different schemes, each with their own strengths and weaknesses.

Removal of bad vectors is normally accomplished through a series of independent criteria. Since outliers often have magnitudes that are far from those expected, as a first cut, an allowable

range of velocities in each direction is often enforced to remove some outliers. This is termed the global histogram operator (Raffel et al., 2007). Additional measures are required since outliers may also have a reasonable magnitude. Because outliers are often caused by poor signal-to-noise ratio in the correlation plane, the “detectability” Q is often used to detect outliers (Keane and Adrian, 1990). Q is defined as the ratio of the largest value in the correlation plane divided by the next largest value. One can better ensure elimination of bad vectors by requiring a large minimum value of Q (e.g., >2), but doing so will result in the elimination of some good vectors and the possibility of biased statistics.

The remainder of rejection criteria postulate some level of “smoothness” to the flow and are based on how the vector in question compares to its neighbors. Early outlier detection methods were commonly based on comparing a vector value to the median of its neighbors (Raffel et al., 2007; Westerweel, 1994). This is an effective method since the median is robust to neighboring spurious vectors. This was improved upon with the “universal outlier detector” (Westerweel and Scarano, 2005) in which the median detector is modified by normalizing each vector residual with respect to the median vector by the median of all residuals.

In some cases, it may be necessary to fill eliminated vectors with a reasonable replacement. This replacement may be an average of neighboring points or may be based on the second or third largest peak in the correlation plane. We note that such replacements likely have a large uncertainty. If a time-averaged result is desired, it may be more accurate to simply eliminate the missing vector and rely on other instances in time to provide data for that location. If instantaneous results are needed, a replacement vector may be more justified.

48.4 Designing a PIV Experiment

Several of the choices that a user must make when acquiring PIV will now be discussed. For each case, guidance is provided to aid in these choices.

48.4.1 Modes of PIV Image Acquisition

PIV data can be acquired in two different operating modes, which are referred to here as time-series mode (TSM) and frame-straddling mode (FSM). Each has distinct advantages and the selected mode may depend on the available equipment, experimental conditions, along with the intended use for the data.

48.4.1.1 Time-Series Mode

In this mode, the camera frames at the same rate that the laser fires and the first vector field is computed from the first and second image, then the second vector field is computed from the second and third image, and so on. This produces $N - 1$ vector fields from N images. The camera and laser-timing sequences are shown in Figure 48.6, which shows that the time between two images is fixed by the relationship: $dt = 1/f_{\text{acq}}$. This means that unlike

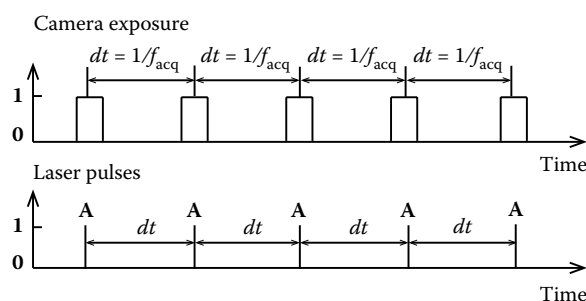


FIGURE 48.6 Description of the laser and camera-timing sequences for TSM PIV with a single-cavity laser. 0: Device not active; 1: device active.

FSM, the acquisition frequency is not independent of the time between frames (dt). Therefore, the acquisition frequency should be selected such that the resulting time between laser pulses, $dt = 1/f_{\text{acq}}$, is adequate for the flow velocities within the FOV to displace the particles several pixels. Assuming f_{acq} is sufficiently higher than the convection speed of the scales of interest in the flow, TSM provides vector fields by which it is possible to observe the time evolution of these flow structures. There exists no fixed criteria for what f_{acq} must be, but a good rule of thumb is to use dt values that are small enough that the flow structures of interest reside in the FOV for 10 consecutive frames. Time-resolved (TR-PIV) data can yield time-related information such as power spectra, Lagrangian tracking, and space-time correlations. Since the consecutive samples of TR data are correlated in time, they are not statistically independent samples. As a result, this mode of acquisition is typically ill-suited for the calculation of velocity statistics such as the time-mean or Reynolds stresses. This point is discussed in detail in George (1978), Benedict and Gould (1996), Lavoie et al. (2007), and Tennekes and Lumley (1972).

There are a number of advantages to acquiring PIV data using TSM. Several of these are a direct result of being able to use a single-cavity laser. A timing sequence for TSM using a single-cavity laser is shown in Figure 48.6. When using a single-cavity laser, there is no need to adjust or optimize the beam overlap. Also, the use of a single-cavity laser results in overall lower variations of laser intensity between individual camera frames. Although some lasers allow for independent control of each of the laser cavities, many higher-speed lasers, especially Nd:YLF (see Section 48.4.4) do not have this capability. Also, a single-cavity laser typically costs 60% of an equivalent dual-cavity laser. Finally, single-cavity lasers that are run in TSM have the smallest timing errors of any lasers used in PIV, as described in the paper by Bardet et al. (2013).

For many PIV systems, the repetition rate of the laser can limit the ability to use TSM. For systems with dual-cavity lasers, the dt can be reduced further by firing the cavities in an alternating cavity mode, which doubles the effective repetition rate of the laser. This timing sequence is shown in Figure 48.7. A typical Nd:YLF laser can pulse at repetition rates up to 10 kHz; therefore, the use of alternating cavities means TSM data rates of up to 20 kHz are possible. Data rates in excess of

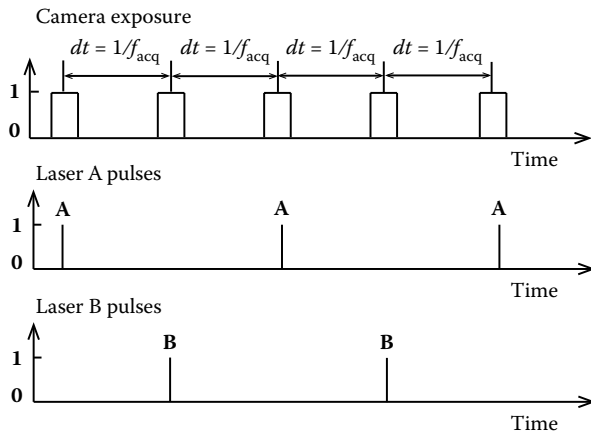


FIGURE 48.7 Description of the laser and camera-timing sequences for TSM PIV with a dual-cavity laser. 0: Device not active; 1: device active.

10 kHz are easily attained by many complementary metal oxide semiconductor (CMOS) cameras, although many of these need a reduced resolution to run at such high speeds (see [Section 48.4.3](#) for more details on this capability). Systems that use flash lamp pumped Nd:YAG lasers can pulse up to 200 Hz; so, data rates up to 400 Hz can be reached using an alternating cavities-timing sequence. The associated dt values are well within the necessary range for TR-PIV data in many liquid flows.

The use of TSM also opens the possibility of using a far-wider variety of cameras since there is no need to have the shutter electronics required for FSM data. Also, unlike FSM, the exposure time of each camera frame is equal and can be adjusted. This shutter control means that the use of band-pass filters can be avoided, decreasing equipment costs and increasing the measured signal intensity of the particles. However, band-pass filters are still helpful for reducing the brighter surface reflections that occur from light scattering off a solid boundary when certain types of coatings are used.

48.4.1.2 Frame-Straddling Mode

In this mode, pairs of images are collected with laser pulse A fired toward the end of the first frame and laser pulse B fired at the beginning of the second frame. This mode decouples the choice of dt from the camera frame rate. FSM mode should be selected when the velocity is too high to be captured using a $dt = 1/f_{acq}$ or when acquiring statistically independent samples is required (see the discussion at the end of this section). Velocity fields are typically less correlated in time than with the TSM described in the previous section. The minimum dt possible is limited only by the interframe time for the camera, which can be as low as 120 ns for the best-performing charge-coupled device (CCD) and scientific complementary metal oxide semiconductor (sCMOS) cameras. High-speed CMOS cameras generally have slower interframe times, typically greater than 1 μ s, although some models can be as low as 500 ns. Some details of FSM using CCD versus CMOS cameras are described in the next two paragraphs.

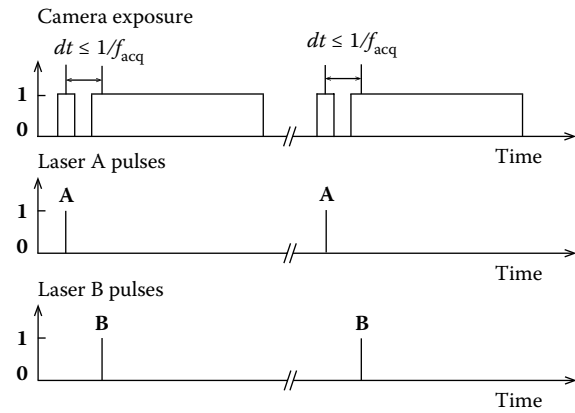


FIGURE 48.8 Description of the laser and camera-timing sequences for FSM PIV with CCD and sCMOS cameras. 0: Device not active; 1: device active.

As shown in Figure 48.8, the exposure for the second frame in FSM is considerably longer than the first frame when a CCD camera is used. This is a direct consequence of the interline transfer architecture of CCD cameras that achieves these low interframe times. The longer second exposure poses problems for PIV data in the presence of room light because the background of the second frame will be significantly brighter than the first frame. These effects can be mitigated by the use of high-transmissivity optical band-pass filters or by collecting data in a room that is completely dark. It should be noted that the longer second exposure is only true only for CCD and sCMOS cameras; the exposures will be equal for CMOS cameras.

A timing sequence for FSM using CMOS cameras is shown in Figure 48.9. Since CMOS cameras can acquire at much faster rates than CCD cameras, the cameras are simply triggered at twice the required data rate. Figure 48.9 shows that the exposure times between consecutive frames are equal, which provides nominally similar intensity levels between each frame in the image pair. Unlike FSM data with a CCD camera, a band-pass filter is not needed to mitigate the effects of a brighter second

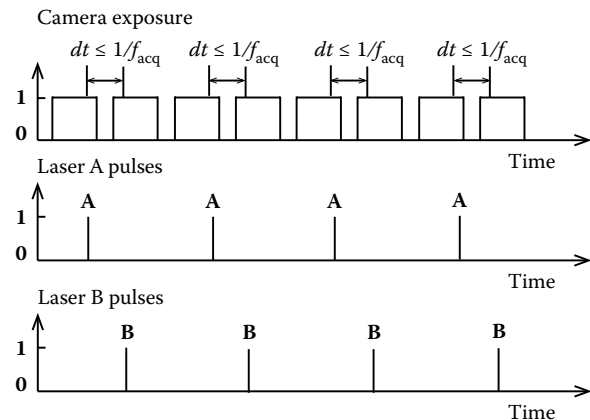


FIGURE 48.9 Description of the laser and camera-timing sequences for FSM PIV with CMOS cameras. 0: Device not active; 1: device active.

frame. The usage of band-pass filters can still be helpful for reducing brighter reflections (from light scattering off a solid boundary) that occur when certain types of surface coatings are used. It should be noted that the maximum frame rate of CMOS cameras is always specified for single-frame rates; so, the data acquisition rate will be exactly half of this maximum rate when using FSM in CMOS cameras.

Although TSM is generally recommended for TR-PIV, it is also possible to use FSM for measuring TR-PIV where the requirement that $dt = 1/f_{acq}$ is not tenable, but its use is limited. For very high velocities and/or smaller FOVs, time correlation between adjacent vector fields disappears completely and, in such cases, the system is simply being used to capture large amounts of data in a short time. An example where this is useful would be in a blow-down wind tunnel where the facility can only be used to acquire data for a very short period of time.

Because TSM systems often have a minimum sampling frequency that may exceed the requirements for independent samples, FSM is best suited for calculating statistical quantities (i.e., mean velocities, Reynolds stresses, turbulence intensity, etc.). This is particularly important in turbulent flows where a high number of statistically independent samples are necessary for properly resolving higher-order moments, as discussed in Lavoie et al. (2007). It is also the preferred mode for flows with high velocities (where dt values must be $< 1/f_{acq}$) and flows where higher spatial resolution is important.

The Nyquist criterion that governs the sampling frequency required to recover frequency information from a signal is opposed to an independent sampling criterion. This is illustrated in Figure 48.10, which shows the same velocity waveform acquired with two different PIV systems. The first is a TSM system (open symbols) with a high f_{act} compared to the time scales of the flow. The second is an FSM system with a smaller f_{act} . While the same number of points were acquired in each case, it

is clear from the figure that averaging the open symbols will not provide an accurate estimate of the velocity average. Sampling longer would improve the estimate of the mean, but not at the rate of $\sqrt{1/N}$, where N is the number of samples, that independent samples provide. An estimate of Reynolds stress will be even more erroneous. Similarly, any attempt to learn about the frequency content of the flow using the FSM system will fail since the sample is badly aliased. In most flows, a single set of measurements will not be suited for computing both statistics and frequency information, such as spectra. Two sets of measurements, and, most likely, two different PIV systems, are required.

48.4.2 Camera Basic: Characteristics of Digital Camera Sensors

Since PIV is most commonly performed using a coherent, monochromatic light source, color information is of no use. Furthermore, color cameras are inherently less sensitive than monochromatic cameras because color filters, which result in significant losses, are used to separate the colors. Therefore, monochromatic cameras are used nearly exclusively for PIV. Scientific-grade cameras typically use either CCD sensors or CMOS sensors. Each of these sensor types have advantages and disadvantages. The preferred type depends on the requirements of the user. A newer type of sensor, sCMOS, is also available. The sCMOS sensor combines the better aspects of both CCD and CMOS sensors using a hybrid technology. Proper selection of a camera requires an understanding of the fundamental characteristics that are common to all digital sensor types. These are discussed in the following sections.

48.4.2.1 Camera Resolution

The resolution of a digital camera is a function of (1) the number of pixels on the sensor and (2) the size of the pixels relative to the

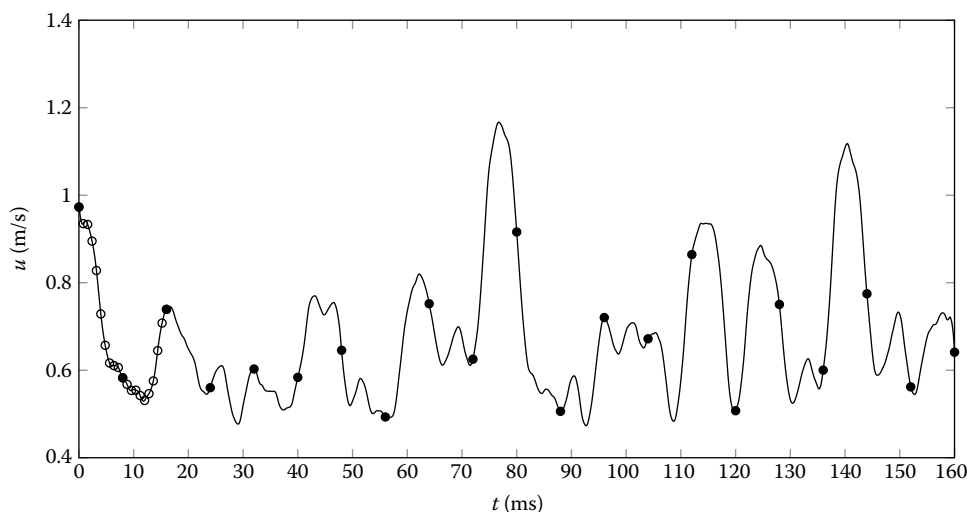


FIGURE 48.10 A PIV time series acquired at a single location using TSM (open symbols) and FSM (closed symbols) at a much smaller f_{act} .



FIGURE 48.11 Image displayed using different spatial resolutions.

projected image. Smaller pixels collect less light but allow for a larger number of pixels to be fit onto the sensor plane. To obtain a satisfactory reproduction of an image, the relative size of the projected image to the pixel size must be considered. Basic sampling theory requires that at least two samples are collected for each resolvable unit, with more samples improving the fidelity of the measurement. In PIV images, pixels that are too large can lead to an undersampling of the tracer particles, which will cause bias errors from peak locking, as discussed in [Section 48.5.3](#). It is important to note that once the size of the image projected onto the sensor is appropriately adjusted as per these sampling requirements, increasing the number of pixels in the sensor will increase the FOV of the image and not the resolution. This point is emphasized in Figure 48.11 where the same image captured at four different resolutions and reproduced at the same size on the page.

48.4.2.2 Camera Dynamic Range

The dynamic range for a camera is a measure of the number of intensity levels that can be recorded by each pixel. Dynamic range is typically defined as the highest measurable signal divided by the lowest measurable signal (i.e., noise) of the sensor. The highest measurement signal is referred to as the full-well capacity and represents the largest charge (specified in the number of electrons, e^-) that a pixel can hold before saturation. When pixels receive charge beyond saturation, a number of spurious effects can result, including the filling of adjacent pixels (blooming) or pixel burnout.

Camera dynamic range can typically be assessed by noting the number of digital bits that are used to describe the output of each



FIGURE 48.12 Images displayed using different bit depths.

pixel. The number of gray levels for each pixel is 2^{bits} . Therefore, a 1-bit camera is black and white while an 8-bit camera has 256 gray levels. Figure 48.12 shows the same image represented at the same resolution but with a varying dynamic range.

In practice for PIV, the laser intensity is normally limited by the full-well capacity of the camera sensor. Once this intensity is set, a better dynamic range allows the camera to perceive dimly lit particles that may be below the noise floor of a less-sensitive camera. One trade-off of a larger bit depth is the expense of transferring and storing the data from the camera. Consequently, bit depth is often sacrificed for transfer speed.

48.4.2.3 Camera Spectral Response and Sensitivity

Digital camera sensors have a response and sensitivity to incoming light that varies depending on the wavelength of that incoming light. This is similar to the behavior of a photographic film, but instead, it is characterized by the performance of the pixels on the array. The sensitivity of a pixel is referred to as the quantum efficiency (QE) and is defined as the ratio between the number of collected photoelectrons and the number of incident photons per pixel. The QE primarily depends on the pixel's architecture: the aperture (commonly referred to as "fill factor"), material, and the thickness of the optically sensitive area. Photons of different frequencies penetrate the sensor differently generating a wavelength-dependent QE for different sensor types. Examples of the QE as a function of wavelength for several different sensors are shown in [Figure 48.13](#). Knowledge of a particular camera's QE is particularly important for PIV because images are collected using a monochromatic light source (typically 532 or 527 nm).

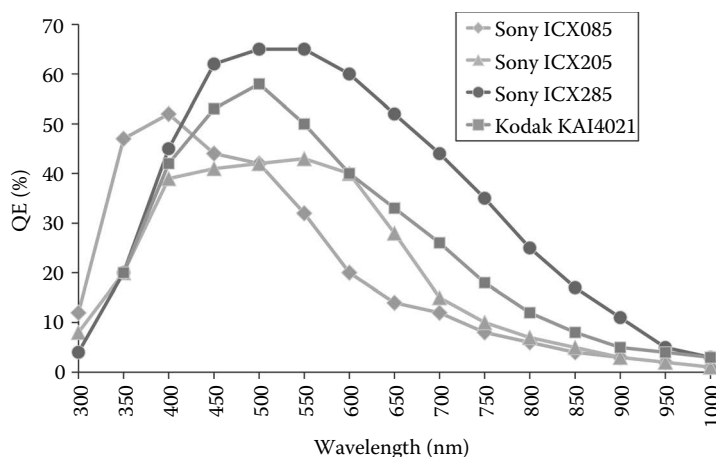


FIGURE 48.13 Spectral response for several different camera sensors.

48.4.3 Camera Types

48.4.3.1 Charged Coupled Device

Since the advent of frame-straddling digital cameras for PIV in the late 1990s, the bulk of these cameras have been based on CCD sensors. CCD cameras offer five distinct advantages for PIV experiments:

- CCD architecture allows for PIV recordings that use FSM to record two images spaced in time by dt values that are as small as 110 ns.
- CCD sensors can easily have high numbers of pixels (up to 29 megapixels for modern scientific-grade chips).
- Cameras using CCD sensors typically have a large dynamic range (12–14 bit).
- CCD sensors have a high sensitivity.
- CCD sensors have small pixels that are on the order of 4–8 μm . The small pixel size also reduces the effects of peak locking.

Images from CCD cameras can be transferred to a computer either via standard computer interfaces such as gigabit Ethernet cable (1 or 10 GbE) or through the use of a framegrabber board (camera link, coaxial, or fiber optic). CCD cameras using gigabit Ethernet interfaces have the advantage of not requiring a framegrabber board, but the slower interface means the download rates to the computer are slower (which subsequently limits acquisition rates). Cameras with the camera link (or CamLink) interface can send images to the computer significantly faster than cameras using standard computer interfaces. An alternative approach is to store the images onto the memory located inside the camera (which are later downloaded to the computer), but this requires expensive camera memory and limits the total number of consecutive images that can be recorded.

Since the advent of 64-bit computer-operating systems, a better approach is to write directly to the computer random access memory (RAM). Using this strategy, a CCD camera using a CamLink interface can write 14-bit, 2-megapixel images

at 15 Hz or greater. These speeds are quite compatible with the typical 15-Hz neodymium-doped yttrium aluminum garnet (Nd:YAG) lasers used in PIV. Images stored on the personal computer (PC) RAM must still be written to the hard drive, which creates another bottleneck for experiments. In situations where fast acquisition and storage are required with no downtime, a redundant array of independent disk (RAID) can be placed in the computer to decrease the write times to the hard drive.

48.4.3.2 Complementary Metal Oxide Semiconductor

Another type of camera is based on sensors using CMOS technology which allows for very fast acquisition rates (over 20 kHz) at modest resolutions (typically 1 megapixel). Although the cost and size of these cameras has decreased in recent years, they are still considerably more expensive and larger than a typical scientific-grade CCD camera. CMOS cameras also generally have a lower sensitivity, lower resolution (1-megapixel typically, with some 4-megapixel models now available), and a lower dynamic range (12 bit) than a standard CCD camera used in PIV. The lower sensitivity is typically compensated for by increasing the pixel size (10–28 μm), which can cause problems with peak locking.

Since there is no interface that can download images faster than a few hertz to the PC, these cameras must have onboard memory to store the images. This memory is expensive and cannot be easily changed or upgraded without sending the camera back to the manufacturer. In most cases, enough memory can be specified to allow for a few thousand images to be stored in a time series. This allows for several seconds of data at their typical (kHz) acquisition rates. Careful consideration must be given to the amount of memory required for the length of the time series that will be recorded. An interesting feature of CMOS cameras is that the resolution can be reduced to boost the acquisition rate. An example of this capability is shown for a typical scientific-grade CMOS camera in Figure 48.14. Despite the high costs and other performance limitations, the high acquisition rates (25–20,000 + Hz) of CMOS cameras make them ideally suited for TR-PIV.

Frame rate (fps)	Resoluion max (pixel)		Record time on 8-GB Memory (s)	Images
	H	V		
1,000	1024	1024	5.46	5457
2,000	1024	1024	2.73	5457
3,000	1024	1024	1.82	5457
5,400	1024	1024	1.01	5457
10,000	768	768	0.97	9701
15,000	768	512	0.97	14,552
20,000	512	512	1.09	21,829

FIGURE 48.14 Table showing the increased speed at reduced resolutions for a generic CMOS camera, along with the length of the time series that can be recorded.

48.4.3.3 sCMOS

A new type of sensor was recently introduced with the intent to provide scientific-grade cameras that employ many of the best features of both CCD and CMOS technology. This hybrid CCD/CMOS architecture is called scientific complementary metal-oxide-semiconductor (sCMOS). Cameras using sCMOS technology have sensors that consist of CMOS readout-integrated circuits (ROICs) that are bump bonded to a CCD-imaging substrate. The first-generation sCMOS cameras have specifications that are superior to typical scientific-grade CCD cameras in several aspects:

- sCMOS architecture allows for PIV recordings that use FSM to record two images with dt values as small as 120 ns.
- sCMOS sensors have resolutions of 5.5 megapixels (smaller than the biggest CCD but larger than any scientific-grade CMOS sensor).
- Cameras with sCMOS sensors have a dynamic range of 16 bit.
- Extremely high sensitivity (read-out noise of $1\text{--}2e^-$), with small pixels ($6.5\text{ }\mu\text{m}$). This small pixel size is also advantageous because it reduces the effects of peak locking.
- Acquisition rates of up to 25 Hz (double-frame images) at full resolution. Similar to CMOS sensors, sCMOS cameras can be reduced in resolution to increase acquisition rates.

The fastest acquisition rates for sCMOS cameras are still well below those of CMOS cameras, which make them impractical for use in TR-PIV experiments. However, their impressive characteristics and relatively fast acquisition rates make them an attractive alternative to scientific-grade CCD cameras.

48.4.4 Lasers

The light source used for PIV is typically a pulsed solid-state laser. Four principal characteristics normally describe these lasers:

- *The optical pump source*—These are characterized by their geometry, spectral irradiance, and temporal performance.

- *The activator ions*—Different activator ions have distinctive charge states and free-ion electronic configurations.
- *The host material*—Each host material has its own mechanical, thermal, and optical properties.
- *Number of cavities*—Since many pulsed lasers fire at rates far below that required for PIV, they are often sold in pairs and called “dual-cavity” lasers.

Additionally, whether the laser is pulsed (via a quality switch [Q-switch] or mode-locking element in the cavity) or continuous wave (CW) is a very important consideration when selecting a laser for a particular PIV experiment. As described in the following sections, the higher peak power and very short pulse width make pulsed lasers the standard light source for PIV. The use of CW lasers is more limited, but can be appropriate in some applications.

48.4.4.1 Pulsed Nd:YAG Lasers

Nd:YAG lasers are the most commonly used solid-state pulsed laser in PIV. They use yttrium aluminum garnet (YAG) crystals with Nd^{3+} ions as the active medium. This combination has properties that are very favorable for laser operation. The YAG is a highly durable host that has a good optical quality and a high thermal conductivity. The cubic structure of YAG is also favorable for a narrow fluorescent linewidth, resulting in high gain and low threshold for laser operation. Nd:YAG lasers are optically pumped using flashtubes or laser diodes. The fundamental wavelength for Nd:YAG lasers is 1064 nm (infrared), but this is frequency doubled by means of special crystals to 532 nm (green light).

The use of a Q-switch inside the laser cavity allows for the laser to be operated in a triggered mode. Q-switches are electro-optical modulators that commonly consist of a Pockels cell and a polarizer. The Q-switch alters the resonance characteristics of the optical cavity. Under careful operation, the laser cavity can resonate at the most energetic point during the flash lamp cycle. This Q-switched mode is quite useful for PIV as it allows for a high-energy, short-duration pulse width to be emitted from the cavity. Typical pulse widths for Nd:YAG lasers are 5–10 ns, making them ideally suited for PIV applications. Nd:YAG lasers are compact and easily transported with pulse

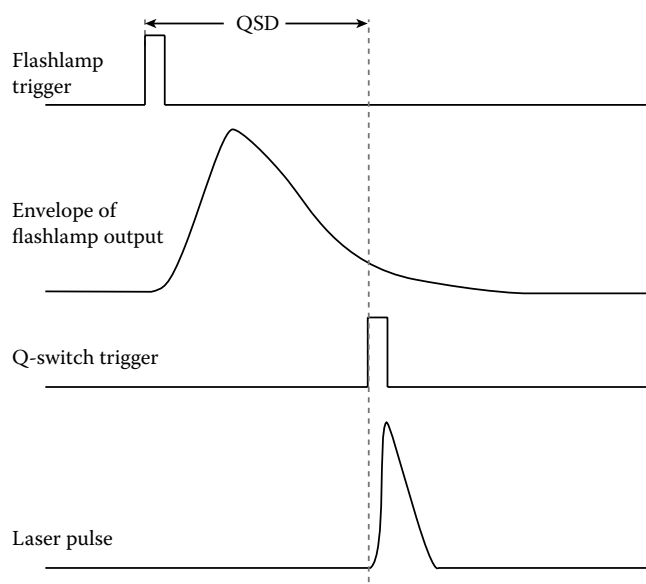


FIGURE 48.15 Diagram showing the relationship between the flashlamp and Q-switch trigger for a Nd:YAG laser.

energies that typically range from 30 to 200 mJ per pulse. Their associated repetition rates can range from a single shot up to around 100 Hz.

Depending on the Nd:YAG manufacturer and model, laser output intensity is controlled by adjusting flash lamp power, timing of Q-switch with respect to the flash lamp pumping, or using an optical attenuator. Optical attenuators come in several forms and can be internal or external to the cavity. To obtain the best beam profile, it is usually recommended that the Q-switch timing be optimized and the flash lamp power be maximized. The only effective method for maintaining the best beam profile while lowering the output energy is through an optical attenuator. However, since many low-cost Nd:YAG lasers sold with PIV systems do not offer an optical attenuator (contained in the laser head), the use of an external optical attenuator is advised. These can be purchased as an after-market item and mounted on the front of the laser. If an external optical attenuator is not available, output power can also be controlled through Q-switch timing (with the consequence of changing the beam profile).

A typical timing scheme is shown in Figure 48.15. Triggers are explained below in Section 48.4.5. The intensity of output light from the laser can be controlled by modifying the interval Q-switch delay (QSD). The figure depicts a low-intensity setting. The intensity could be increased by shortening the QSD. Light is emitted from the laser shortly after the Q-switch trigger and the output is very brief compared to the timescales of PIV.

48.4.4.2 Pulsed Nd:YLF Lasers

Another choice for the host medium of neodymium is YLF (yttrium lithium fluoride). Solid-state Nd:YLF lasers are optically pumped using laser diodes, yielding a fundamental wavelength

of 1054 nm. This fundamental wavelength is converted into the visible spectrum using frequency doublers as described for Nd:YAG lasers. The resulting visible spectrum is 527 nm (green light). The Nd:YLF material has some advantages over Nd:YAG, particularly when it is diode pumped. In Nd:YLF diode pumping, the fluorescence lifetime is twice as long as in Nd:YAG. Since laser diodes are power limited, a larger pump time resulting from the longer fluorescence time provides roughly twice the energy storage from the same number of diodes. Continuously pumped Nd:YLF lasers can achieve repetition rates from a single shot to 10 kHz.

The Q-switches are acousto-optic modulators where the refractive index of the crystal is modulated by pressure exerted by radio frequency (RF) acoustic waves. This Q-switching principle allows for the higher repetition rates, but it also yields pulse widths that are considerably longer than those of flash-lamp-pumped Nd:YAG lasers, typically between 150 and 350 ns. Even with these longer pulse widths, these lasers are well-suited for a wide range of gas and liquid flows.

48.4.4.3 DPSS-CW Lasers

Another type of solid-state laser is the diode-pumped solid-state laser (DPSS). Here, a solid gain medium such as ruby or Nd:YAG crystal is continuously pumped using a laser diode. In the case of an Nd:YAG crystal, the resulting light is 1064 nm and is then frequency doubled to 532 nm. These lasers have no Q-switches and are therefore not operated in a pulsed mode, but instead emit a continuous output beam (also called a CW output). Their output is typically specified in watts, with commercially available lasers ranging from 100 mW to 10 W. Since their energy output for a short time duration is much lower than for pulsed lasers, they are typically limited to low Reynolds number flows in liquids, where larger diameter or silver-coated particles can be used.

48.4.5 Timing

A PIV system requires a series of precisely timed “triggers” that fire the lasers at the appropriate intensity, ensure that each frame of the camera is properly illuminated, and specify dt . A trigger is a digital signal, simply meaning that it is normally near 0 V volts and rises suddenly to a value typically near 5 V when turned on. Most triggered hardware can use either the leading (rising) edge of a pulse or the trailing (falling) edge. For the sake of this chapter, we will assume that the leading edge is being used. The exact voltage of the high and low state is not critical, nor is the duration of the high state. This explanation is specific to Q-switched pulsed laser systems (such as dual-cavity Nd:YAG laser-based systems as described in Section 48.4.4), although much of the discussion applies to other systems.

These digital signals can be generated by a digital card inside the acquisition computer or by external hardware. Firing the lasers requires four digital signals and additional signals are required for the camera’s image acquisition. A timing sequence is shown in Figure 48.16. The acquisition sequence is begun by

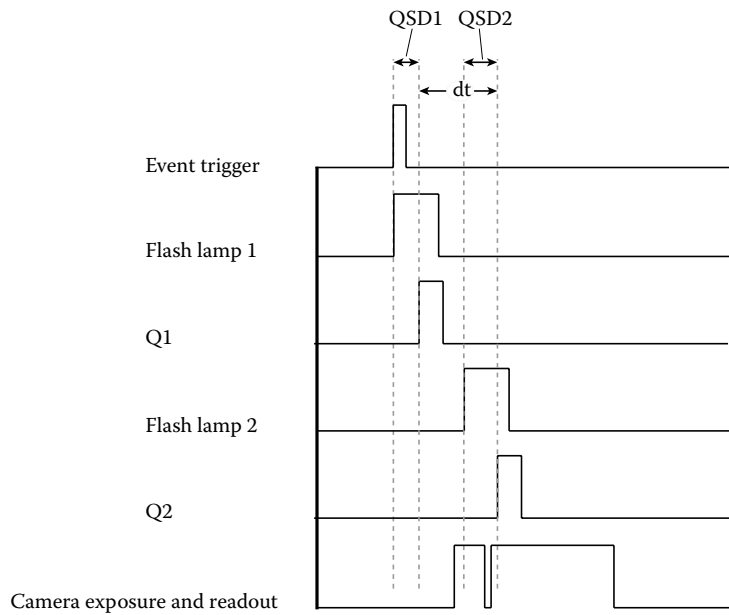


FIGURE 48.16 Diagram showing the various pulse trains that must be generated to run a PIV system.

an event trigger that may be external to the PIV system or could be generated by the acquisition computer if the starting time is not critical. Immediately upon receiving this trigger, the flash lamp on Laser 1 is fired. The Q-switch on Laser 1 is fired at a delay time (QSD1) on the order of 100 ms after the flash lamp, and the duration of this delay controls the intensity of Laser 1. The Laser 2 flash lamp and Q-switch are fired such that the delay between them (QSD2) results in the desired intensity of Laser 2 and so, the desired delay between the two images dt is formed by Q1 and Q2.

This delay is normally between a fraction of a microsecond and the frame period of the camera. A fifth signal is usually required to start the camera's acquisition and begin the exposure of the camera sensor for the first image. The start and end time of the sensor exposure are not critical as long as the Q-switch (and thus the laser) fires inside it. For some cameras, a second pulse may be required to cause the camera to off-load the data and start a new exposure for the second image, while on other models this may occur automatically after some fixed period of time. Some acquisition systems may also require that additional pulses be sent to the frame grabber to control the off-loading of data.

Jitter in the QSD1 and QSD2 delays will cause the laser intensity to vary from shot to shot. Jitter in the dt delay is much more serious, since the velocity measurements resulting from PIV are $d\vec{x}/dt$. In most cases, this is only a serious concern if very small dt values are specified.

48.4.6 Tracer Particles for PIV Seeding

The appropriate choice of tracer particles in PIV is of critical importance. PIV is based on the measurement of the displacement over time (i.e., velocity) of tracer particles in the flow. It is therefore of critical importance that the particles accurately

follow the flow to ensure the fluid velocity is properly measured. Their ability to do so depends on their size and density. Moreover, the proper choice of particles can help to improve the overall imaging conditions and mitigate experimental challenges (low laser energy density, high background noise, etc.).

48.4.6.1 Particle Dynamics and Particle Response Times

Since PIV relies on the particles following the flow, the assumption of being "neutrally buoyant" is critical to the fidelity of PIV measurements. This requires that the gravitational forces arising from a mismatch between the particle density, ρ_p , and the fluid density, ρ_f are minimized. The gravitationally induced velocity, U_g from Stokes' drag law arises from a particle (with a diameter d_p) under acceleration (in this case from gravity, g). This relationship assumes spherical particles in a viscous fluid, characterized by the dynamic viscosity μ_f at low Reynolds number (all of which are valid assumptions for most PIV experiments). Following Stokes' theorem, this is expressed as

$$U_g = \frac{d_p^2(\rho_p - \rho_f)}{18\mu_f}g \quad (48.4)$$

This requires selection of particles that are close in density to the surrounding fluid. Given that the density of the particles will always be slightly different, choosing smaller-diameter particles can also help to ensure the particles are following the flow. The selected diameter, in the case of Mie scattering, should not be so small that the imaged intensity is insufficient. This will be discussed in the following section.

The degree to which the particles do not follow the flow can be characterized by the slip velocity, u_s , which is defined as the difference between the particle velocity and the velocity of the

surrounding fluid. An estimate of the slip velocity was derived by Raffel et al. (2007), using an analogy to Equation. 48.4:

$$U_s = U_{sp} - U_f = \frac{d_p^2(\rho_p - \rho_f)}{18\mu_f} \frac{du_p}{dt} \quad (48.5)$$

Using Equation 48.5, it is clear that slip velocity can be made minimal by either minimizing the particle diameter, d_p , the particle acceleration, du_p/dt , or the density ratio of the particles, ρ_p/ρ_f . Minimizing particle diameter is practical only up to a point, since the choice of usable particles does not have an unlimited range of sizes. Similarly, the particle acceleration depends on the flow being measured. Since turbulent flows with strong gradients are of particular interest, this also only can be controlled up to a point. The requirement of *neutrally buoyant* particles is the most important consideration for how a particle follows the flow. The density ratio can be rewritten to define neutrally buoyant particles as those with the condition $(\rho_p - \rho_f)/\rho_f \ll 1$. This condition can be more easily satisfied for liquid flows ($\rho_p/\rho_f \approx 1$) than for gas flows ($\rho_p/\rho_f \gg 1$).

If non-neutrally buoyant particles are used, the particles may not follow the flow resulting in errors in PIV measurements. The degree of mismatch that may be tolerated depends on the accelerations contained in the flow. Shocks and strong vortices generate such large accelerations. An example of the latter is shown in Figure 48.17.

Determining how well the particles follow the flow can be quantified by the *relaxation time* τ_p , which is defined as the response time of the particle to sudden changes in the fluid velocity. Using the form of Equation 48.4, this is defined as

$$\tau_p = \frac{d_p^2(\rho_p - \rho_f)}{18\mu_f} \quad (48.6)$$

From Equation 48.6, small values for the relaxation time are desired to ensure the particles are reliably follow the flow. Turbulent flows are typically characterized by strong velocity gradients and regions of shear. Care must be given when considering the choice of the particle with respect to the timescale of a specific turbulent flow. This can be characterized by analyzing the Stokes number for the particle, S_k , which is defined as the ratio of the relaxation time and the characteristic timescale of the flow, τ_{flow} :

$$S_k = \frac{\tau_p}{\tau_{flow}} \quad (48.7)$$

Following the recommendations of Samimy and Lele (1991), $S_k \leq 0.05$ (with $S_k = 0.2$ yielding a 2% error).

48.4.6.2 Mie Scattering

The majority of particles used in PIV images rely on scattered light via Mie scattering. The term “Mie scattering” refers to the Mie (or also the Lorenz–Mie) solution to Maxwell’s equation,

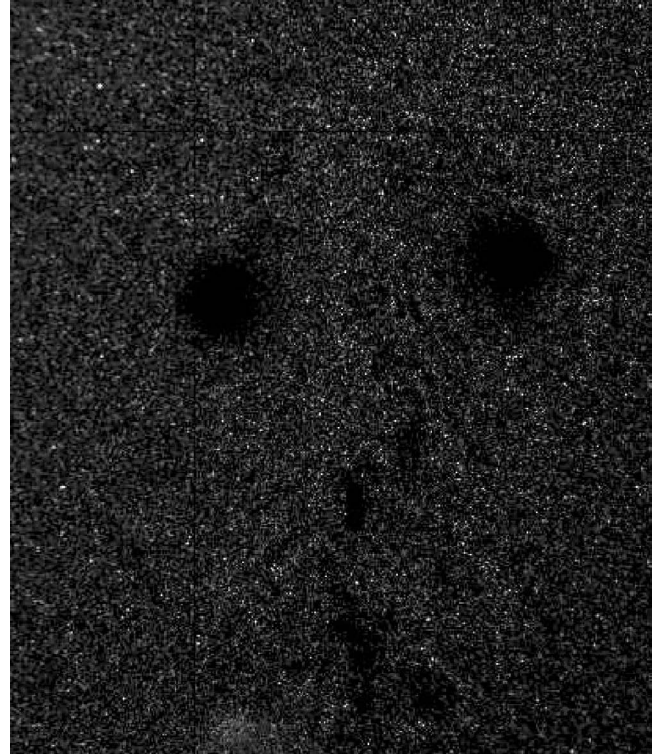


FIGURE 48.17 PIV data of a synthetic jet. A vortex ring is present in the center of the image and has caused the seed particles to leave the region of the vortex core due to high acceleration. The particles are olive oil droplets formed in a Laskin nozzle and are likely on the order of a micron in diameter. (From Smith, B. L. and Smith, D. R. 2014. Chapter 3: Measurement techniques for synthetic jets and results. In *Synthetic Jets: Fundamentals and Applications*, Mohseni, K. and Mittal, R. (eds), CRC.)

which describes the scattering of electromagnetic radiation by a sphere. The solution, which is an infinite series, can be evaluated using computer programs such as MiePlot (Laven, 2014). In Mie scattering, the scattered light intensity depends on the particle diameter, the wavelength of the light, and the refractive index of the particle material relative to the refractive index of the surrounding medium. In the Mie regime, where $d_p > \lambda$, the scattered light intensity is approximately proportional to the surface area (i.e., d_p^2) of the particle.

Mie scattering plots are often presented in polar form, as shown in Figure 48.18 for typical PIV particles used in water and Figure 48.19 for typical PIV seeding in air flows. These figures show that the portion of scattered light in the forward direction, between 0° and 45° (commonly referred to as “forward scattering”), is very large. A significant, albeit smaller, portion of the light is scattered in the backward direction, between 135° and 180° , which is correspondingly referred to as “backward scattering”.

It is interesting to note that single-camera PIV normally operates at a scattering angle of 90° , where the intensity of scattered light is relatively quite low. These plots illustrate why PIV needs a much stronger light source than LDV, which normally operates in a near-forward or near-backward scattering mode.

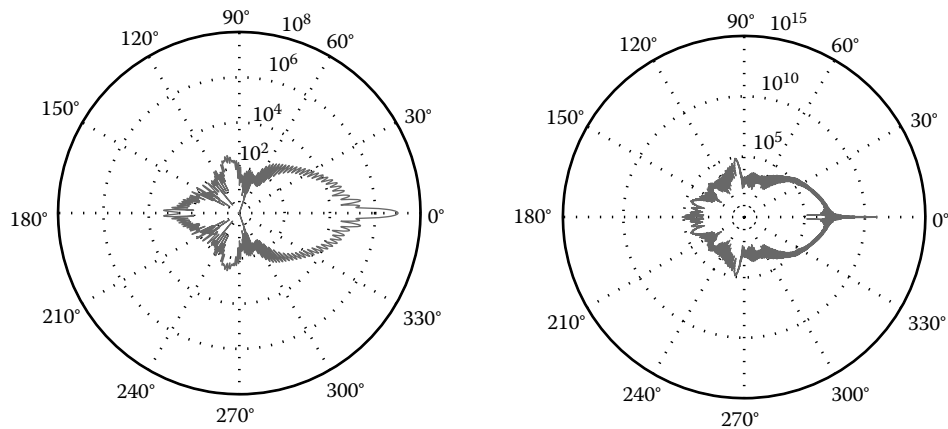


FIGURE 48.18 Mie scattering for hollow glass spheres in water ($m = 1.14$) (left — $D_p = 10 \mu\text{m}$, right — $D_p = 100 \mu\text{m}$).

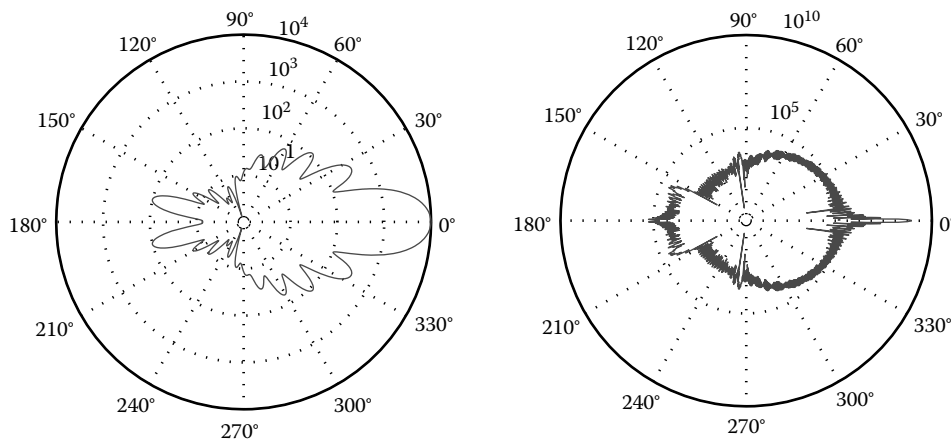


FIGURE 48.19 Mie scattering for olive oil droplets in air ($m = 1.47$) (left — $D_p = 2 \mu\text{m}$, right — $D_p = 20 \mu\text{m}$).

A well-designed SPIV experiment can also take advantage of near-forward or near-backward scattering, which will dramatically increase the signal-to-noise ratio for a given combination of camera, light source and associated camera, and light sheet optics.

48.4.6.3 Particles for Mie Scattering

Seed particles used in gases are generally not used in liquids and vice versa. Most commonly, liquid drops are used as seed particles in air. Some examples of materials used are shown in Table 48.1. These generally have a much larger density than gas and therefore must be very small (near $1 \mu\text{m}$) to follow the flow. There are two main options for liquid seeds for tracer particles in gas: oil atomizers and foggers. Several atomizer types have been discussed by Melling (1991); Kahler et al. (2002); and Kahler (2003) and of these, for typical use, the Laskin nozzle and “reference” nozzle are perhaps the easiest to implement. Kahler concludes that the reference nozzle, which is a Laskin nozzle without a collar surrounding the air jets, performs nearly identically to a Laskin nozzle, meaning that the collar serves no purpose. In addition to simplicity and low cost, the particle generator can operate at

high pressure, allowing particle injection into high pressure. Nontoxic oil, such as olive oil, works well in these generators. The mean particle diameter is near $1 \mu\text{m}$ and can be manipulated somewhat through the geometry and input pressure.

Foggers are generally proprietary devices designed for theater effects. While these so-called “theatrical foggers” provide an inexpensive method to seed large volumes of air, their wide range of particle diameters ($5\text{--}80 \mu\text{m}$) make them nonideal for PIV measurements. These theatrical foggers also can be messy to work with and leave large amounts of material coating the wind tunnel. They use proprietary fluid composed of purified water and glycerol, which is added as a liquid, then heated, and pumped to form an aerosol.

An alternative to theatrical foggers exists in a higher-grade version designed specifically for scientific use. Although these are more expensive than the theatrical foggers, their uniform particle size ($1\text{--}2 \mu\text{m}$) and ease of use make them superior. Scientific-grade foggers use a fluid composed of approximately 70% glycerol (BP/USP Garde) and 30% deionized water. Other models are available that use a white mineral oil (a consideration

TABLE 48.1 Summary of Commonly Used Particles for PIV in Gases

Material	Type	ρ_p (kg/m ³)	d_p (μm)	Reference
DEHS	Liquid	912	1–2	Kähler et al. (2002)
Olive oil droplets	Liquid	970	1–3	Ragni et al. (2011)
Glycerol–water	Liquid	1078	1–2	Neal et al. (2014)
TiO ₂	Solid	4230	0.01–0.5	Ragni et al. (2011)
Helium bubbles	Gas	Neutral	300	Scarano et al. (2014)

when deicing properties of glycols/glycerols are a concern). These foggers use a compressed can to form the aerosol and generate very little residue buildup. The cost of a scientific-grade fogger is very comparable to oil atomizers.

Choosing between an oil atomizer and a scientific-grade fogger can come down to several considerations (since both deliver 1–2 μm particles, use safe liquids, and have very minimal buildup on experimental facilities). Foggers tend to be better for seeding large volumes for a relatively short period of time, such as would be required for an open-loop tunnel. With these devices, it is possible to flood the upstream plenum and deliver a very homogeneous mixture into the test section. In contrast, oil atomizers tend to deliver a lower (yet steady) supply of particles that last for a longer period of time. Oil atomizers are therefore often preferred for closed-loop wind tunnels and other facilities that can recirculate the air supply. Additionally, foggers can be run simply with a standard air-conditioning (AC) outlet, whereas oil atomizers typically require pressurized shop air to run.

For very large FOV or for thick, low-intensity laser sheets, helium-filled soap bubbles (HFSB) have recently been used for tracer particles (Scarano et al., 2014). While earlier work had concluded that HFSBs do not track the flow well, these authors showed that by using a smaller HFSB (about 300 μm), acceptable results are possible.

Seeding for liquid flows is generally less challenging since it is possible to obtain neutrally buoyant particles for a wide range of fluids. The most commonly used particles are hollow glass spheres, which have the advantage of low cost and a wide range of bulk densities since the wall thickness of the bubbles may be controlled during their manufacture. Some examples are shown in Table 48.2. Since they are neutrally buoyant, one may use much larger particles than for air flows, which results in much better light scattering, as shown above. Alternatives to Mie-scattered particles are also possible, as discussed in the next section.

48.4.6.4 Solid Particles (Non-Mie Scattered)

Solid particles can be used instead of Mie-scattered particles in both liquid and gas flows. In each case, the motivations for their use can be quite different. However, caution must be given in the design of the experiment as the properties of Mie-scattering (i.e., near-forward or near-backward scattering) are no longer available to the user.

In gas flows that involve either high temperatures or reactive environments, the seeding material used in either oil atomizers or scientific-grade foggers will not survive long enough to record

TABLE 48.2 Summary of Commonly Used Particles for PIV in Liquids

Material	Type	ρ_p (kg/m ³)	d_p (μm)	Reference
Hollow glass spheres	Solid	1005	10	Raffel et al. (2007)
Polyamide	Solid	1003	20–100	Adrian and Westerweel (2011)
PMMA	Solid	1190	1–100	Adrian and Westerweel (2011)

PIV data. In these cases, solid particles made of metal oxide powders such as titanium dioxide (TiO₂), alumina (Al₂O₃), and silica (SiO₂) are recommended. Additional details can be found in Raffel et al. (2007); Raffel et al. (2011); and Schroeder and Willert (2008).

Since powders tend to form agglomerates, creating a controlled dispersion of these particles is a challenging task. The delivery device must either break up the agglomerates or remove them from the aerosol prior to delivering the dispersion into the facility. A novel and often-cited approach to remove the agglomerates comes from Wernet and Wernet (1994). In cases where a liquid-particle suspension is not feasible, a suspension can also be created directly from the dry powder through the use of a fluidized bed. This approach can also be used in elevated pressure applications as described in Willert and Jarius (2002) and Willert et al. (2006). A good overview of dispersing solid particles into gases for PIV can be found in Melling (1991).

In liquid flows, the condition of neutral buoyancy is easily met by a wide range of solid particle materials, including polyamide and TiO₂. Another possibility in liquid flows is to gain even more reflected light (but not Mie scattering) by using the more reflective silver-coated glass spheres. The wide range of diameters for different materials that meet the neutrally buoyant criterion in liquid flows provides many possibilities for effective PIV seeding.

48.4.6.5 Fluorescent Particles

An alternative to Mie scattering is the use of fluorescent particles as tracers. Fluorescent particles shift the wavelength of the incident light (typically laser light that is in the green spectrum) to a higher wavelength. This principle makes fluorescent particles extremely useful in flows where there is a high amount of scattered light from solid surfaces (i.e., near wall regions). Other examples include experiments where it is necessary to distinguish the particles to be measured from other particles in the FOV (i.e., multiphase flows and micro-PIV applications). Fluorescent particles are used in combination with an optical filter on the camera to block the scattered light below a certain wavelength.

The process of fluorescence involves exciting molecules into a rotational state that reemits light at higher wavelengths than the excitation wavelength. Because this process also involves a loss of energy, fluorescence is sometimes referred to as “inelastic scattering.” The intensity of the fluorescent signal is typically overall weaker than that of Mie-scattered particles. Fluorescent intensities do vary as a function of the intensity of the illumination, I_0 , the number of dye molecules in the particle, N_M , the

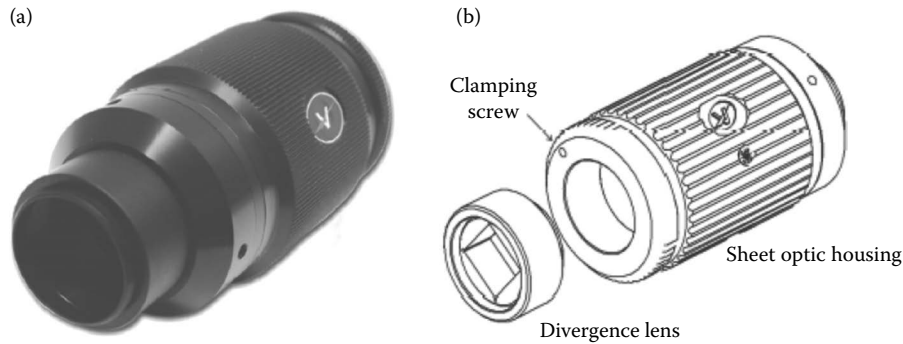


FIGURE 48.20 Compact sheet optics used for creating PIV light sheets.

absorption of the dye (at the incident light wavelength, $\alpha [\lambda_0]$), and the emissivity of the dye (at the emitted light wavelength), $\epsilon (\lambda_e)$. This relationship is expressed as

$$I_e = I_0 \alpha \epsilon N_M \quad (48.8)$$

Because fluorescence involves the volume of the fluorescent molecules that are contained within the particle volume, I_e is typically proportional to d_p^3 unless the incident light cannot reach into all parts of the particle interior or if dye concentration is not high and the emitted light is subsequently reabsorbed.

The higher density of fluorescent particles limits them to water and other liquid flows for PIV. Furthermore, commercially available versions of these particles are typically available as aqueous suspensions. Dry fluorescent particles are also available, but normally only at larger diameters, $d_p > 7 \mu\text{m}$. To date, no references exist on the successful use of fluorescent particles in gas flows. Additionally, the high cost of fluorescent particles usually restricts them to smaller-scale (liquid) flows. However, Pedocchi et al. (2008) discusses a simple technique for making large, inexpensive batches of fluorescent particles for use in large-scale water flow experiments. The use of Equation 48.8 shows the parameters that can maximize the intensity of the fluorescent signal from homemade particles.

48.4.7 Optics

Once a laser has been selected, the next step is to select an appropriate set of optics to convert the laser beam into a light sheet (or in the case of volumetric measurements, a laser volume). The focus of this section is to describe the basic elements needed to form a light sheet appropriate for a PIV experiment. A compact set of optics commonly used for PIV is shown in Figure 48.20. Other solutions exist, and the basic components are described in the following sections. For additional and more advanced configurations, several good resources can be found including (Raffel et al., 2007; Adrian and Westerweel, 2011).

48.4.7.1 Aperture Angle

The essential optical component required to generate a light sheet is a cylindrical lens. For lasers with a sufficiently small

beam diameter and divergence, a thin light sheet can be made from this single component. However, this is rarely the case with most standard pulsed PIV lasers (e.g., Nd:YAG and Nd:YLF). In these cases, additional optical components are required, as discussed in the next section.

The relationship between the aperture angle α , focal length of the cylindrical lens, f , and the beam diameter, d at the location of the lens is:

$$\tan(\alpha/2) = d/2f \quad (48.9)$$

as shown in Figure 48.21. This relationship does not account for the beam divergence, which is generally negligible for the purpose of estimating the aperture angle. Cylindrical lenses for creating light sheets are typically diverging lenses, described by a negative focal length. Typical values used in PIV are $f = -10, -20$, and -50 mm . Using Equation 48.9, it can be shown that for a fixed beam diameter, α increases with increasing (absolute value) of f . The choice of a cylindrical lens depends on the distance from the laser beam output to the FOV and the required size of the FOV. An incorrect choice will result in failure to fully illuminate the FOV, or illumination of a large area outside the FOV, which results in a nonoptimal use of the laser pulse energy.

48.4.7.2 Lens Configuration

The majority of lasers used in PIV (Nd:YAG and Nd:YLF) have too large a beam diameter to use a single cylindrical lens. These

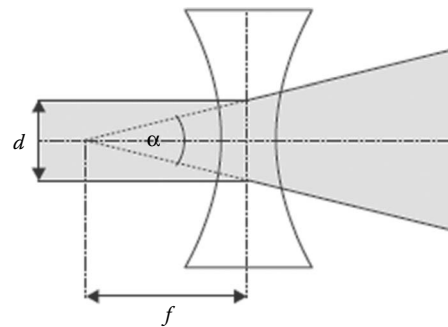


FIGURE 48.21 Schematic showing the aperture angle, α , focal length, f , and beam diameter, d .

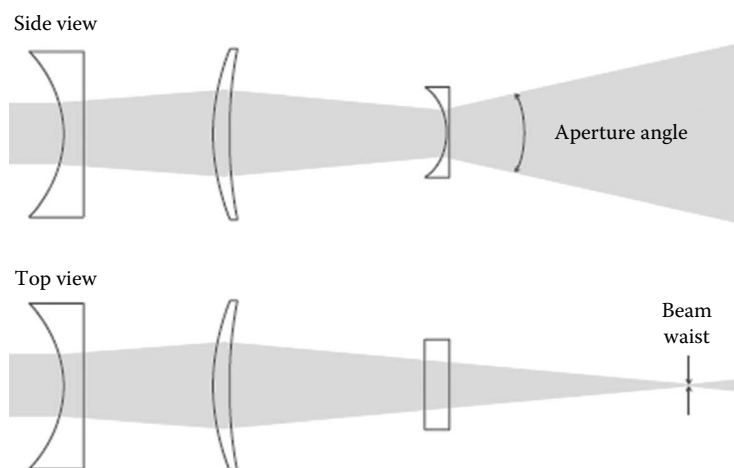


FIGURE 48.22 Lens configuration for forming a PIV light sheet.

light sources require additional optical components to create a thin light sheet with a high-energy intensity. A minimum of one additional lens is required to generate a thin beam waist for the light sheet. Since PIV applications often require short focal lengths, a common way to thin the light sheet is to add a two-telescope lens in combination with a cylindrical lens. One such example is shown in Figure 48.22.

Here, the use of two spherical lenses creates a compact set of sheet optics. A diverging lens is used first to avoid focal lines in the vicinity of the lenses. A focal point in a high-powered pulsed laser can cause the air nearby to ionize. Also, dust particles can burn and burn spots can appear if dust is on the surface of the optics. In addition to these reasons, the beam properties of the laser will be undesirably altered by the acoustic radiation from the focal lines. For this reason, a closed housing, as shown in Figure 48.20, is desirable. This arrangement can be assembled into a compact form that is quite convenient for use in most labs, or alternatively, for use in the field where setting up an optical table is not possible.

Figure 48.23 shows that light sheet thickness can be varied by adjusting the spacing between the two spherical lenses. Optimizing the light sheet thickness is of critical importance for creating a thin plane for PIV measurements. This thin plane will maximize the laser energy density required to achieve high intensities of scattered light from the particles. Since both the light sheet thickness and the aperture angle (as described above in Figure 48.21 and Equation 48.9) vary with distance from the laser output, the adjustment of the focal length to optimize the light sheet thickness must be considered concurrently with the correct aperture angle.

The use of coated optics (coated for the wavelength of the laser light) is advised. Uncoated lenses will reflect a small percentage of light from the surface. Although the amount of reflectivity is often small (4%–5%), the use of multiple lenses can cause the transmitted light to be quickly reduced. Reflected light can cause damage if it focuses near the surface of other optical components.

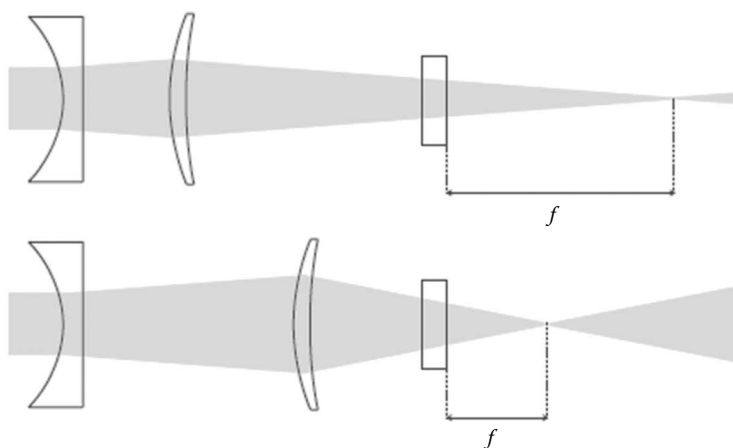


FIGURE 48.23 Changing the focal length through lens spacing.

48.5 Best Practices for Good Measurements

This section will describe how to choose some basic parameters of a PIV measurement and provide guidance on how to control several aspects of the measurement.

48.5.1 Choosing the Time between Images dt

Selection of dt directly impacts the dynamic range of the measurement by controlling the size of the particle displacements. Dynamic range is improved as dt becomes larger, but at some point (which is specific to a given setup and flow), increasing dt will result in an unacceptable loss of correlated particle images in the two interrogation windows. This is manifest by “bad” or “spurious” vectors, especially in regions of large velocity. With window shifting/deformation and successively reduced interrogation sizes, very large displacements are possible for laminar flow. Turbulent flow results in random through-plane motions that will result in loss of particles that appear in both images. Window shifting/deformation does not mitigate these effects.

It is commonly stated that PIV displacements should be approximately 1/4 of the interrogation region size. With window shifting or deformation, this is only true for the first pass. A typical scheme is to start with a large interrogation region for which the particle displacement is less than 1/4 of D_p , and reduce the interrogation region size in successive passes to improve the spatial resolution of the measurement.

Insufficient displacement (due to too small dt) limits the dynamic range of the measurement and increases the relative random error (Boillot and Prasad, 1996). Random error has the effect of inflating Reynolds stress values, since these measure real velocity fluctuations as well as measurement noise. It has been shown by Wilson and Smith (2013) that particle displacements of at least five pixels are required to find accurate Reynolds stresses even under ideal conditions.

As the dt becomes larger, two detrimental effects can occur. The most obvious is that there may be insufficient particle images in both interrogation regions for the first pass, in which case the algorithm will fail and a spurious vector will be generated. This is easily detected by observing the number of bad vectors in the field. A more subtle effect is error due to acceleration (Boillot and Prasad, 1996). One can test to see that random error does not change with dt by testing multiple values of increasing dt and using the smallest value for which the Reynolds stress values remain constant.

48.5.2 Choosing Interrogation Region Size

With modern multipass predictor-corrector PIV algorithms, one must choose the initial and final interrogation region size. Guidance on how to do so can be found in Raffel et al. (2007) and will be repeated here. The choice of the final interrogation region size is a trade-off between cross-correlation signal strength and spatial resolution. Since the cross-correlation is formed

by pairs of particle images that appear in both time instances, larger interrogation regions provide more particle images in each image, which, in turn, improves the correlation strength. Smaller interrogation regions require increased seeding density to provide sufficient correlation strength. However, one cannot arbitrarily raise the seeding density. Too much particle image overlap will cause speckle patterns for which correlation analysis is not valid. For a tolerable particle density, one can reduce the final interrogation size until an unacceptable number of spurious vectors are generated as a result.

For the initial interrogation pass, one must choose a size that captures the full dynamic range of the displacements within the FOV by observing the one-quarter rule, which requires that the maximum particle displacement is approximately 1/4th the size of the interrogation region. In some instances, too large of an initial interrogation region size in the presence of small eddies can be detrimental as the motion within the interrogation region is highly nonuniform. This can diminish the correlation strength resulting in a bad vector in the predictor step, thus causing the algorithm to fail.

48.5.3 Adjusting Particle Image Diameter

The diameter of particle images strongly impacts the accuracy of PIV in several ways. If the particle image diameter is on the order of one-camera pixel, the velocity will be strongly biased toward integer displacements due to the well-known peak-locking effect (Fincham and Spedding, 1997; Westerweel, 1997). This error is a bias since its value is repeatable for the same input, but its effects can appear random in a turbulent flow.

Theoretically, the random error of the PIV correlation increases with particle image diameter (Prasad et al., 1992). An optimal particle image diameter near two pixels is now widely accepted.

In many cases for PIV measurements, the particle image size is a weak function of the particle diameter and primarily depends on the magnification M and numerical aperture or $f\#$. Smaller $f\#$ (larger aperture) results in smaller particle images. Owing to diffraction effects, for an ideal case, the image of a particle has a diameter of (Adrian and Westerweel, 2011; Raffel et al., 2007)

$$d_\tau = \sqrt{(Md_p)^2 + d_{\text{diff}}^2} \quad (48.10)$$

where d_p is the particle size, M is the magnification of the image (the ratio of the domain size to the sensor size), λ is the wavelength of light, and

$$d_{\text{diff}} = 2.44 f\# (M + 1) \lambda \quad (48.11)$$

Therefore, for the diffraction-limited case (meaning $d_{\text{diff}} > d_\tau$), it is a simple matter to optimize the particle image diameter by modifying the aperture. Note that changing the $f\#$ changes the amount of light reaching the sensor, which can be compensated by altering the laser pulse intensity. Changing the $f\#$ also

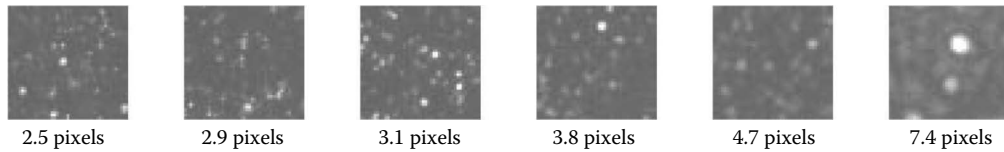


FIGURE 48.24 Images showing how particle image size varies with the lens aperture. All particles in this series of images had similar diameter. (From Wilson, B. M. and B. L. Smith. 2013. *Measurement Science and Technology* 24(3), 035302.)

alters the depth of field, δz , which is defined as the thickness of the region containing in-focus particles in the measurement volume. The depth of field is defined as (Raffel et al., 2007)

$$\delta z = 4.88 \left(\frac{M + 1}{M} \right) f_s^2 \lambda \quad (48.12)$$

Figure 48.24 shows examples of particle images with increasing d_t taken from Wilson and Smith (2013). In that study, the particle image diameter was varied by modifying the f_s of the camera lens and modifying the laser intensity such that the average illumination level remained unchanged.

48.5.4 Seed Image Density

Seed density has a strong impact on the number of valid vectors (Keane and Adrian, 1990, 1992) as well as measurement uncertainty (Timmins et al., 2012; Wilson and Smith, 2013). The probability of a valid vector is a function of the number of particle images that appear in each image of the pair. Therefore, more seed is required for smaller interrogation regions and thinner laser sheets.

Some PIV software comes with front-end tools to estimate the particle image density before acquisition. There are many schemes for doing this, including peak counting or the more-robust autocorrelation-based density (Warner and Smith, 2014). In the absence of these, one can simply zoom in to a region of similar size to the final interrogation region and count the

visible particles, assuming that the density is not so high as to cause a significant particle overlap. In the case where particle overlap is significant, the seeding density is likely sufficient to ensure that its exact value is not important. According to Keane and Adrian (1992), at least five particle images should appear in each image to ensure no spurious vectors. The uncertainty of the measurement decreases with increasing particle image density (Timmins et al., 2012; Wilson and Smith, 2013) until the speckle limit is reached, meaning that particle motion can no longer be detected. This limit depends on the particle image size (Adrian and Westerweel, 2011).

Some example images of different particle densities are shown in Figure 48.25. Each image is captioned with the particles per square pixel as determined for a series of larger images using the method of Warner and Smith (2014). The average number of particles in an average interrogation region is the caption value multiplied by D_I^2 . All these samples are acceptable for $D_I = 64$, but for $D_I = 32$, to obtain five pixel images per interrogation region, one needs at least 0.005 *ppp* and at least 0.02 for $D_I = 16$.

48.5.5 Determining Origin

Given the optical nature of PIV, it can be extremely difficult to know where a measurement lies in space. The simplest methods of determining the location is if an object of known location appears in the raw images. However, such an object typically generates a flare when struck by the laser sheet, obfuscating the location of the object. If one attempts to determine the location

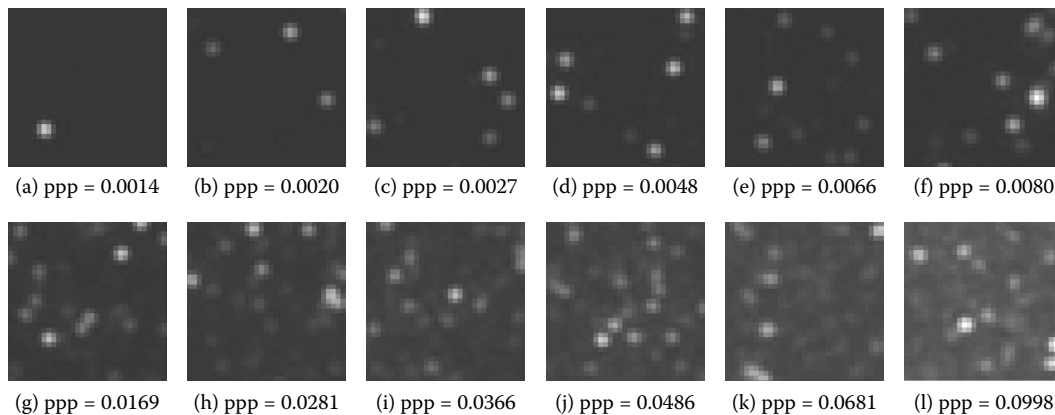


FIGURE 48.25 Images with varying particle image densities. Each image is 32 pixels in each direction. (From Warner, S. O. and B. L. Smith. 2014. *Measurement Science and Technology* 25(6), 065201.)

of an object with illumination other than the laser sheet, one risks locating the object in a plane other than the laser plane. Flow features (e.g., the linear viscous sublayer in a turbulent flow) may be helpful in locating a wall. This issue becomes even more problematic for SPIV (cf. Section 48.6) for which changes in the laser plane location appear identical to changes in the x plane.

48.5.6 Illumination Issues

48.5.6.1 Laser Beam Overlap

As discussed in Section 48.4, many pulsed laser systems consist of two lasers in a single package with both beams steered through the same aperture. For such systems, it is important to ensure that the two beams are well aligned. Failure to do so results in the laser sheets illuminating either different y - or z -locations, depending on the direction of misalignment. Since the laser sheet is spread into the x - y plane by the sheet optics, misalignment in the y direction causes the Gaussian light distribution of one laser to be centered at a larger y value than the other leading to intensity mismatch. This situation should be corrected, but normally does not lead to important problems, assuming that all areas of both images are sufficiently illuminated.

For extreme cases of z misalignment, the two images may illuminate different particles resulting in loss of correlation. This is easily detected by viewing the two images with a very small dt . For cases where there is significant mean flow in the z direction, one may deliberately displace one sheet relative to the other to counter the effect of the through-plane motion.

48.5.6.2 Laser Beam Shape

Ideally, laser beams have a Gaussian distribution, meaning they are brightest in the center and become more dim in each direction in a symmetric manner. This has many important and sometimes subtle ramifications for PIV. Since the beam is converted into a sheet by optics prior to entering the measurement region, the y center of the sheet is illuminated most brightly. Moreover, the sheet intensity is distributed in z in a Gaussian manner, meaning that particles near the center of the sheet are illuminated more brightly than particles away from the sheet z center. The z shape of the sheet has important effects when there is motion through the plane. As discussed in Nobach and Bodenschatz (2009), particle image overlap coupled with the intensity variation through the sheet leads to increased random error. We also note that as solid-state lasers age, the beam shape often becomes distorted.

48.5.6.3 Intensity Matching

The standard dual-cavity PIV lasers (Nd:YAG or Nd:YLF) are actually composed of two independent laser systems that are combined via beam-combining optics. These two laser systems are often controlled through a single laser head controller. The laser head controller will sometimes allow for independent control of the two beam profiles, but often will not. It is common to have variations in the beam profile, energy intensity, and, in

some cases, the pulse envelope. This can be generally classified as “event matching” and includes the effects of out-of-plane motion, differences in overall laser intensity, and differences in beam profile (evidenced in low-frequency spatial variations in laser intensity).

48.5.7 Image Preprocessing

Preprocessing of images can mitigate issues with a PIV setup with little cost. One can remove background images that may bias the velocity to zero displacement or remove the effects of intensity mismatch between the two images or across the image. In the former case, a background image is typically subtracted from all the PIV images. The background image should be formed separately for the first and second images of pairs and can simply consist of the average of the series of data images. Since this average will contain contributions from all particle images in the data set, which are random, a better approach is to form the background based on the minimum intensity observed for each pixel over the set of images. When a particle image is present, that pixel will report a large value and will not be included. Most PIV software includes routines to obtain this minimum field. If one has images that were acquired with one shot more illuminated than the other, this may be corrected through normalization of the images based on their mean and the local intensity fluctuations.

48.6 Stereo Particle Image Velocimetry

SPIV uses two cameras at angles less than 90° to the laser sheet to detect flow normal to the sheet and thus produce all three components (3Cs) of velocity on a two-dimensional (2D) plane (Soloff et al., 1997; Willert, 1997; Prasad, 2000). For this reason, these measurements are also referred to as planar 3C measurements. A schematic of a simple SPIV setup is shown in Figure 48.26. In general, the two cameras can be at any angle and do not need to be on the same side of the laser sheet. Increasing the angle between the cameras has a tendency to decrease the random error in the z velocity component while increasing the random error in the x and y components of velocity. Total angles between 60° and 90° are recommended (Adrian and Westerweel, 2011). SPIV calibration reduces the perspective and magnification error but introduces other error sources. The resampling of the original images required for “dewarping” (i.e., using the calibration to map the image back to an undistorted grid) alters particle image shape and generates errors that could become important if the resultant particle image size becomes larger in one direction. Calibration errors may result in velocity biases or in location errors of the vectors.

While an SPIV system costs roughly twice as much as a 2C system, many feel that SPIV should be the standard system. Since the majority of flows of scientific and engineering interest are turbulent in nature, 3C measurements are often necessary. The increased capital expense and expense of use (e.g., much more

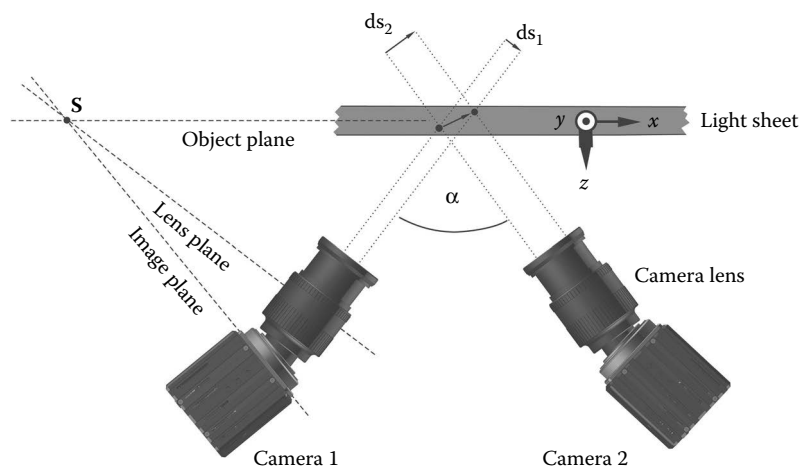


FIGURE 48.26 Schematic of a simple SPIV setup.

complicated calibration procedures, double the storage requirements, and more than double the computational expense) is offset by elimination of the perspective error and random errors due to through-plane motion.

48.6.1 SPIV Optics

To obtain images where the entire plane is in focus in spite of the off normal viewing angle, it is necessary to use a device known as a “Scheimpflug adapter,” which allows the camera body and lens to be positioned at independent angles as shown in Figure 48.26. The user must iteratively find the “Scheimpflug condition,” at which lines passing through the laser plane, the lens plane, and the sensor plane all intersect at point s . Typically, the camera is aimed at a calibration target composed of a grid of dots placed in the laser plane. The user attempts to focus on dots on each side of the image simultaneously and adjusts the lens angle until this is true. Some Scheimpflug adapters simply couple the camera to the lens, while others provide a mounting screw and the camera and lens are cantilevered off both sides of the adapter (see Figure 48.27). The latter type makes alignment simpler by maintaining the FOV while the adapter is adjusted. Performing this task with a large lens aperture (small $f_{\#}$) is recommended since this will form the minimum level of focus for the data that will be acquired.

Quite often, a camera from a stereo setup must look through large changes of the index of refraction. For instance, the camera may sit in air while viewing water inside an aquarium or water tunnel. If the side of the aquarium forms an angle of less than 90° with the camera lens, it is possible that the images will suffer from spherical aberration (astigmatism) that causes the particle images to distort. In most cases, the images are stretched in one direction and the random error in that direction increases as a result (Adrian, 1986). An example is shown in Figure 48.28a.

These effects can be mitigated by placing a prism filled with the same fluid as the experiment working fluid as shown in Figure 48.29. The use of such a prism causes the distorted particle images shown in Figure 48.28a to appear like those in Figure 48.28b.



FIGURE 48.27 Scheimpflug adapter between a digital camera and SLR lens. This type of adapter provides a mounting point so that the angle can be adjusted without changing the lens potions (and thus the FOV).

The viewing wall of the prism is parallel to the principle plane of the lens in order to reduce the combined effects of off-axis viewing with refraction at the air–window–water interfaces.

The Scheimpflug adapter allows for the raw PIV images to stay in focus across the entire FOV, similar to 2C-PIV images. The images will still show a perspective effect, which is accounted for via a calibration function (described in Section 48.6.2). The image pair from each camera are then dewarped using the calibration function to generate a 2C vector field.

48.6.2 SPIV Calibration

Prior to measurement, calibration images acquired at multiple z -locations are used to map “world” locations to locations on each camera sensor. This calibration data are either used to “dewarp” the PIV images into world coordinates prior to correlation (Scarano, 2004), or are used to map the 2C vector fields from each camera into common world locations (Soloff et al., 1997). The calibration procedure is a mapping of space; so errors in stereo calibration are errors in space that may manifest

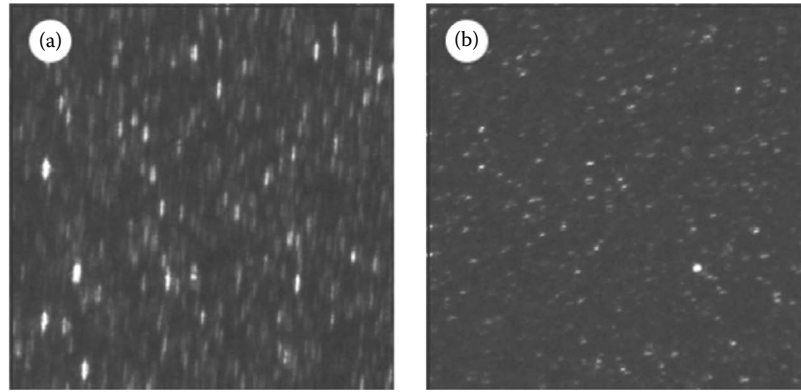


FIGURE 48.28 Particle images from (a) a camera in air looking through a glass wall at an angle substantially less than 90° into water and (b) a camera looking through a prism filled with the same fluids (water) as the flow facility.

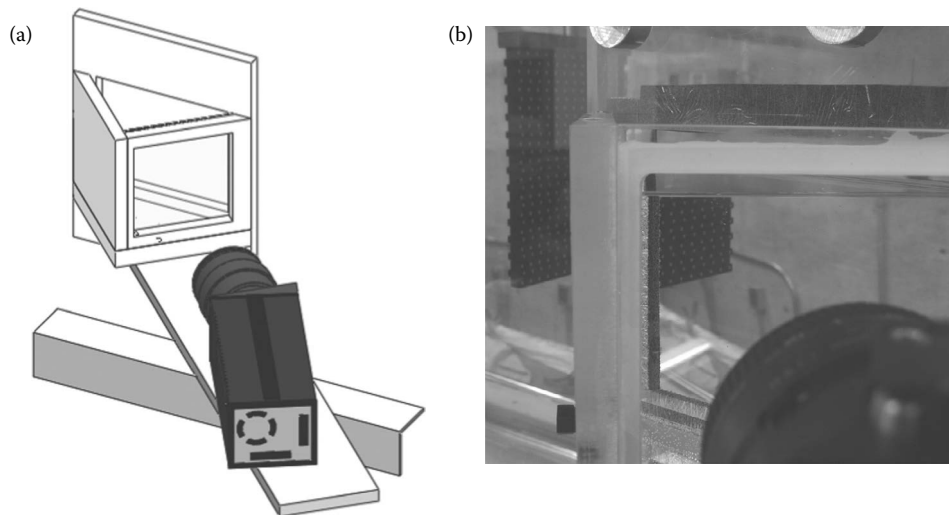


FIGURE 48.29 (a) Line drawing and (b) photograph of a liquid-filled prism attached to a flow facility wall to ensure that all interfaces with a large change in the index of refraction are normal to the camera lens. (Images courtesy of C. Vanderwel, 2014.)

themselves as velocity errors in the presence of a velocity gradient. Stereo calibration begins with the acquisition of images of a calibration plate made of a grid of crosses or dots of known spacing and size. Knowing the location of the marks provides a way to map from locations on the camera sensor to locations in real space. Two models are commonly used to fit calibration data: the pinhole model and the polynomial (general) fit. Some features of these models are now discussed.

48.6.3 Pinhole Calibration Model

In a distortion-free imaging system, all object and image locations can be connected by straight lines that pass through a single point in the camera called the pinhole. Since many setups have appreciable distortions, this idealized case is not always practical. Distortions are introduced by imperfections in the lens, refraction caused by interfaces, and misalignment of the image plane and the object plane (Grant, 1997). Willert (2006)

assessed the performance of three versions of the pinhole camera model and found that a larger number of calibration images or more complex models do not always improve the results. He also showed the choice of a model has little influence on the estimate of the pinhole position when distortion is small and that the marker position estimates are the largest source of random error.

In general, a pinhole calibration model should only be used when there is no change in the index of refraction along the optical path (i.e., normally best for an experiment in air with either no viewing window or a very thin viewing window). This limitation is a result of the pinhole model not accounting for changes in the index of refraction. The pinhole model is therefore not practical for most experiments in liquid flows (since the camera is not directly immersed in the flow and viewing windows are inevitably required). An advantage of the pinhole model is that the calibration functions can be extrapolated beyond the FOV of the original calibration plane, allowing for the calibration target to be smaller than the measurement FOV.

48.6.4 Polynomial Calibration Model

The polynomial (or general) calibration model uses second- or third-order polynomials to map the object and image locations. A second-order model involves 12 unknown parameters determined using a least-squares approach if six or more image-object points are available. Lens distortions or other image nonlinearities can be accounted for by using higher-order terms (Willert, 1997). For a two-camera, stereo setup, about 22 parameters are needed to specify the pinhole models, compared to 80 parameters for the third-order polynomial calibration. An important difference between a polynomial calibration and a pin-hole model calibration is that the parameters in the polynomial calibration have no physical interpretation. This lack of a physical meaning makes it more difficult to determine the quality of a particular calibration when the polynomial method is used.

A polynomial calibration can be used in general for almost any experiment, including those that have changes of the index of refraction along the optical path. It is important for the calibration target to extend across the entire measurement FOV, since extrapolating a polynomial calibration can yield undesirable results. This limitation, along with the required number of parameters, suggests that the calibration target must be chosen carefully for each experiment.

48.6.5 Stereo Self-Calibration

Additional errors can be introduced when the calibration plane and image plane are not aligned. The effect of this misalignment can be seen when comparing simultaneous dewarped images from both cameras. If the calibration and image planes are aligned, the two images should match perfectly. It is not possible to ensure that the laser plane and calibration plane are coincident even under the best of circumstances. Fortunately, this misalignment can be mitigated through self-calibration (Wieneke, 2005). Self-calibration relies on the fact that the dewarped images from each camera contain images of many of the same particles. By performing cross-correlation of the images from each camera, one can determine the relative alignment of the two images as a function of space in the data plane. The map of this misalignment is called a “disparity map.” For the simple case of a z translation of the laser plane relative to the calibration plane, the disparity field is uniformly horizontal (see Figure 48.30).

48.6.6 SPIV Reconstruction

Ultimately, SPIV is based on computing the 2D2C field on a regular grid and using the two interpolated vectors to compute the 3C vector field at regular world grid positions. Once a mapping function has been determined, the 2D3C vector field can be found. Three main approaches for computing the 2D3C vector field have been outlined by Wieneke (2005). These approaches include

1. Computing 2C vector fields using raw images acquired from each camera and interpolating vector values from each 2C vector field onto a common world grid (Prasad, 2000).

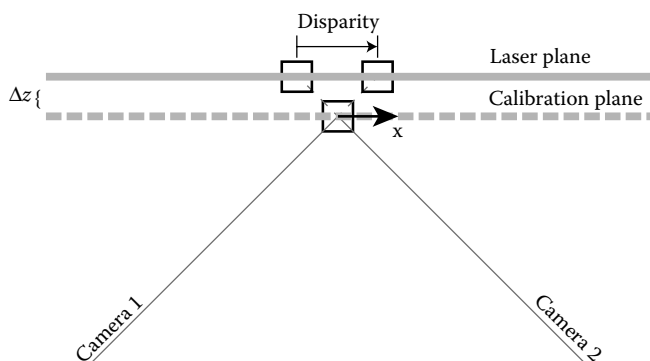


FIGURE 48.30 Sketch demonstrating how a z shift in the laser sheet position becomes an x disparity in SPIV.

2. Computing the 2C vectors using raw images at locations that correspond to a specified location on the world grid (Zhang, 2000).
3. Dewarping raw images and computing 2C vectors at specified world grid positions (Willert, 1997).

The first method does not require much computation time; however, it introduces increased error due to the smoothing that occurs when the vectors are interpolated (Zhang, 2000). The second method does not require interpolation, but requires interrogation window sizes that vary between the two cameras due to perspective effects (Heikkila and Silvén, 1997). The third method does not require interpolation or varying window sizes when mapping, but does require the use of image resampling, which leads to image degradation.

References

- Adrian, R. J. 1986. Image shifting technique to resolve directional ambiguity in double-pulsed velocimetry. *Applied Optics* 25(21), 3855–3858.
- Adrian, R. J. 1991. Particle-imaging techniques for experimental fluid mechanics. *Annual Review of Fluid Mechanics* 23(1), 261–304.
- Adrian, R. J. 2005. Twenty years of particle image velocimetry. *Experiments in Fluids* 39, 159–169.
- Adrian, R. J. and J. Westerweel. 2011. *Particle Image Velocimetry*. Cambridge University Press, New York.
- Bardet, P., M. André, and D. R. Neal. 2013. Timing errors in laser-based transit-time velocimetry. *10th International Symposium on Particle Image Velocimetry – PIV13 Delft*, The Netherlands, July 2–4, 2013.
- Benedict, L. H. and R. D. Gould. 1996. Towards better uncertainty estimates for turbulence statistics. *Experiments in Fluids* 22, 129–136.
- Blois, G., J. L. Best, G. H. Sambrook Smith, and R. J. Hardy. 2014. Effect of bed permeability and hyporheic flow on turbulent flow over bed forms. *Geophysical Research Letters* 41(18), 6435–6442.

- Boillot, A. and A. Prasad. 1996. Optimization procedure for pulse separation in cross-correlation PIV. *Experiments in Fluids* 21(2), 87–93.
- Bosbach, J., M. Kühn, and C. Wagner. 2009. Large scale particle image velocimetry with helium filled soap bubbles. *Experiments in Fluids* 46(3), 539–547.
- Charonko, J. J. and P. P. Vlachos. 2013. Estimation of uncertainty bounds for individual particle image velocimetry measurements from cross-correlation peak ratio. *Measurement Science and Technology* 24(6), 065301.
- Drucker, E. G. and G. V. Lauder. 1999. Locomotor forces on a swimming fish: Three-dimensional vortex wake dynamics quantified using digital particle image velocimetry. *Journal of Experimental Biology* 202(18), 2393–2412.
- Fincham, A. and G. Spedding. 1997. Low cost, high resolution DPIV for measurement of turbulent fluid flow. *Experiments in Fluids* 23(6), 449–462.
- Frank, D. M., J. E. Ward, S. E. Shumway, B. A. Holohan, and C. Gray. 2008. Application of particle image velocimetry to the study of suspension feeding in marine invertebrates. *Marine and Freshwater Behaviour and Physiology* 41(1), 1–18.
- George, W. K. 1978. Processing of random signals. In *Proceedings of the Dynamic Flow Conference*, Johns Hopkins University, Baltimore, MD, pp. 757–800.
- Grant, I. 1997. Particle image velocimetry: A review. *Proceedings of the Institution of Mechanical Engineers, Part C: Journal of Mechanical Engineering Science* 211(1), 55–76.
- Heikkilä, J. and O. Silvén. 1997. A four-step camera calibration procedure with implicit image correction. In *Computer Vision and Pattern Recognition, 1997. Proceedings, 1997 IEEE Computer Society Conference*, San Juan, Puerto Rico, pp. 1106–1112. IEEE.
- James, J. F. 2011. *A Student's Guide to Fourier Transforms: With Applications in Physics and Engineering*. Cambridge University Press, Cambridge.
- Kahler, C. 2003. General design and operating rules for seeding atomisers. In *5th International Symposium on Particle Image Velocimetry*, Busan, Korea, pp. 1–7.
- Kahler, C., B. Sammler, and J. Kompenhans. 2002. Generation and control of tracer particles for optical flow investigations in air. *Experiments in Fluids* 33, 736–742.
- Keane, R. D. and R. J. Adrian. 1990. Optimization of particle image velocimeters. I. Double pulsed systems. *Measurement Science and Technology* 1(11), 1202.
- Keane, R. D. and R. J. Adrian. 1992. Theory of cross-correlation analysis of PIV images. *Applied Scientific Research* 49(3), 191–215.
- Klewicki, J. 2007. Measurement considerations in wall-bounded turbulent flows: Wall shear stress. In C. Tropea, A. L. Yarin, and J. F. Foss (eds.), *Springer Handbook of Experimental Fluid Mechanics*. Springer-Verlag, Berlin, Heidelberg.
- Laven, P. 2014. Mieplot v4.3, <http://www.philiplaven.com/mieplot.htm>.
- Lavoie, P., G. Avallone, F. De Gregorio, G. Romano, and R. Antonia. 2007. Spatial resolution of PIV for the measurement of turbulence. *Experiments in fluids* 43(1), 39–51.
- McNutt, M. K., R. Camilli, T. J. Crone, G. D. Guthrie, P. A. Hsieh, T. B. Ryerson, O. Savas, and F. Shaffer. 2012. Review of flow rate estimates of the deepwater horizon oil spill. *Proceedings of the National Academy of Sciences* 109(50), 20260–20267.
- Melling, A. 1991. Tracer particles and seeding for particle image velocimetry. *Measurement Science and Technology*, 8(12) 1406–1415.
- Neal, D. R., A. Sciacchitano, B. L. Smith, and F. Scarano. 2015. Collaborative framework for PIV uncertainty quantification: The experimental database, *Measurement Science and Technology* 26(7), 074003.
- Nobach, H. and E. Bodenschatz. 2009. Limitations of accuracy in PIV due to individual variations of particle image intensities. *Experiments in Fluids* 47(1), 27–38.
- Pedocchi, F., J. E. Martin, and M. H. García. 2008. Inexpensive fluorescent particles for large-scale experiments using particle image velocimetry. *Experiments in Fluids* 45(1), 183–186.
- Persoons, T. and T. S. O'Donovan. 2011. High dynamic velocity range particle image velocimetry using multiple pulse separation imaging. *Sensors* 11(1), 1–18.
- Prasad, A. K. 2000. Stereoscopic particle image velocimetry. *Experiments in Fluids* 29(2), 103–116.
- Prasad, A. K., R. J. Adrian, C. C. Landreth, and P. W. Offut. 1992. Effect of resolution on the speed and accuracy of particle image velocimetry interrogation. *Experiments in Fluids* 13(2–3), 105–116.
- Raffel, M., C. E. Willert, S. T. Wereley, and J. Kompenhans. 2007. *Particle Image Velocimetry*. Springer-Verlag, Berlin, Heidelberg.
- Ragni, D., F. Schrijer, B. Van Oudheusden, and F. Scarano. 2011. Particle tracer response across shocks measured by PIV. *Experiments in Fluids* 50(1), 53–64.
- Samimy, M. and S. Lele. 1991. Motion of particles with inertia in a compressible free shear layer. *Physics of Fluids A: Fluid Dynamics (1989–1993)* 3(8), 1915–1923.
- Scarano, F. 2002. Iterative image deformation methods in PIV. *Measurement Science and Technology* 13(1), R1–R19.
- Scarano, F. 2003. Theory of non-isotropic spatial resolution in PIV. *Experiments in Fluids* 35(3), 268–277.
- Scarano, F. 2004. A super-resolution particle image velocimetry interrogation approach by means of velocity second derivatives correlation. *Measurement Science and Technology* 15(2), 475.
- Scarano, F., S. Ghaemi, G. Caridi, J. Bosbach, U. Dierksheide, and A. Sciacchitano. 2014. On the use of helium-filled soap bubbles for large-scale tomographic PIV wind tunnel experiments. In *17th International Symposium on Applications of Laser Techniques to Fluid Mechanics*, Lisbon, Portugal.

- Scarano, F. and P. Moore. 2012. An advection-based model to increase the temporal resolution of PIV time series. *Experiments in Fluids* 52(4), 919–933.
- Schroeder, A. and C. E. Willert. 2008. *Particle Image Velocimetry: New Developments and Recent Applications*, volume 112. Springer, Berlin, Heidelberg.
- Sciacchitano, A., D. R. Neal, B. L. Smith, S. O. Warner, P. P. Vlachos, B. Wieneke, and F. Scarano. 2015. Collaborative framework for PIV uncertainty quantification: Comparative assessment of methods. *Measurement Science and Technology* 26(7), 074004.
- Sciacchitano, A., F. Scarano, and B. Wieneke. 2012. Multi-frame pyramid correlation for time-resolved PIV. *Experiments in Fluids* 53(4), 1087–1105.
- Sciacchitano, A., B. Wieneke, and F. Scarano. 2013. PIV uncertainty quantification by image matching. *Measurement Science and Technology* 24(4), 045302.
- Smith, B. L. and D. R. Smith. 2014. Measurement techniques for synthetic jets and results. In *Synthetic Jets: Fundamentals and Applications*, Chapter 3, Mohseni, K. and Mittal, R., CRC.
- Soloff, S. M., R. J. Adrian, and Z.-C. Liu. 1997. Distortion compensation for generalized stereoscopic particle image velocimetry. *Measurement Science and Technology* 8(12), 1441.
- Tennekes, H. and J. L. Lumley. 1972. *A First Course in Turbulence*. MIT Press, Cambridge, MA.
- Timmins, B. H., B. M. Wilson, B. L. Smith, and P. P. Vlachos. 2012. A method for automatic estimation of instantaneous local uncertainty in particle image velocimetry measurements. *Experiments in Fluids* 53, 1133–1147.
- Vanderwel, C. 2014. *Turbulent Diffusion in Uniformly Sheared Flow*. PhD thesis, University of Ottawa.
- Warner, S. O. and B. L. Smith. 2014. Autocorrelation-based estimate of particle image density for diffraction limited particle images. *Measurement Science and Technology* 25(6), 065201.
- Wernet, J. H. and M. P. Wernet. 1994. Stabilized alumina/ethanol colloidal dispersion for seeding high temperature air flows. *Proceedings of ASME Symposium on Laser Anemometry: Advances and Applications*, Lake Tahoe, NV, 19–23 June 94, pp. 32983.
- Westerweel, J. 1993. *Digital Particle Image Velocimetry—Theory and Application*. PhD dissertation, TU Delft.
- Westerweel, J. 1994. Efficient detection of spurious vectors in particle image velocimetry data. *Experiments in Fluids* 16(3–4), 236–247.
- Westerweel, J. 1997. Fundamentals of digital particle image velocimetry. *Measurement Science and Technology* 8, 1379–1392.
- Westerweel, J., D. Dabiri, and M. Gharib. 1997. The effect of a discrete window offset on the accuracy of cross-correlation analysis of digital PIV recordings. *Experiments in Fluids* 23(1), 20–28.
- Westerweel, J. and F. Scarano. 2005. Universal outlier detection for PIV data. *Experiments in Fluids* 39, 1096–1100.
- Wieneke, B. 2005. Stereo-PIV using self-calibration on particle images. *Experiments in Fluids* 39(2), 267–280.
- Wieneke, B. 2015. PIV uncertainty quantification from correlation statistics. *Measurement Science and Technology*, 26(7), 074002.
- Willert, C. 1997. Stereoscopic digital particle image velocimetry for application in wind tunnel flows. *Measurement Science and Technology* 8(12), 1465.
- Willert, C., C. Hassa, G. Stockhausen, M. Jarius, M. Voges, and J. Klinner. 2006. Combined PIV and DGV applied to a pressurized gas turbine combustion facility. *Measurement Science and Technology* 17(7), 1670.
- Willert, C. and M. Jarius. 2002. Planar flow field measurements in atmospheric and pressurized combustion chambers. *Experiments in Fluids* 33(6), 931–939.
- Willert, C. E. 2006. Assessment of camera models for use in planar velocimetry calibration. *Experiments in Fluids* 41(1), 135–143.
- Wilson, B. M. and B. L. Smith. 2013. Uncertainty on PIV mean and fluctuating velocity due to bias and random errors. *Measurement Science and Technology* 24(3), 035302.
- Zhang, Z. 2000. A flexible new technique for camera calibration. *IEEE Transactions on Pattern Analysis and Machine Intelligence* 22(11), 1330–1334.